

Siddarth Shankar Das<sup>1</sup>, Nabarun Poddar<sup>1,2</sup>, Veenus Venugopal<sup>1,2</sup>, S Abhilash<sup>3</sup>, and V Rakesh<sup>3</sup>

<sup>1</sup>Space Physics Laboratory, Vikram Sarabhai Space Centre

<sup>2</sup>Department of Physics, University of Kerala

<sup>3</sup>Advanced Centre for Atmospheric Radar Research, Cochin University of Science and Technology

March 25, 2024



26 present configuration of radar can provide a better understanding of three-dimensional  
27 structures of turbulence and instabilities.

28 **[Keywords:** ST radar, aspect-sensitivity, Kelvin-Helmholtz-instability]

29

### 30 **Plain language summary**

31 Radar backscatter from the atmosphere depends directly on the turbulent scale sizes  
32 present and the probing frequency. When the backscatter echo strength decays with the  
33 radar viewing zenith angle, the signals are said to be aspect sensitive i.e., dependent on  
34 the viewing angle. There can be few circumstances under which such characteristics are  
35 observed, all primarily being anisotropic scattering processes which are caused due to  
36 various processes in the atmosphere. Such aspect sensitivity must be quantified for  
37 realising the accurate operation of a radar which would otherwise result in  
38 underestimation of winds and other parameters obtained from the radar. Here the aspect  
39 sensitivity characteristics of the 205 MHz stratosphere–troposphere (ST) radar installed  
40 at Cochin (10.04°N, 76.33°E) are studied using a detailed experiment using various  
41 probing techniques during Indian Summer Monsoon season and the characteristics of the  
42 atmosphere during that period are probed to explain the aspect sensitivity.

43

44

45

46

47

48

49

50

## 51 **1. Introduction**

52 A backscatter echo power and its characteristics are strongly controlled by the  
53 nature of the scatterers present in the atmosphere. A very-high frequency (VHF) radar  
54 echoes are known to be aspect sensitive in general owing to either thin stable layer  
55 providing sharp refractive index gradient or shear driven steep layer structures. The  
56 main mechanisms are isotropic and anisotropic turbulence and Fresnel  
57 reflection/scattering (e.g., Hocking et al., 1986, 1990; Jain et al., 1997; Das et al., 2008).  
58 Unlike isotropic scattering, anisotropic scattering mechanisms lead to a deterioration of  
59 the signal with increasing off-zenith angle, thus rendering the echoes ‘aspect sensitive’  
60 (Röttger and Liu, 1978; Jain et al., 1997). Such aspect sensitivity effectively alters the  
61 radar parameters such as beam pointing angle and hence the quantities derived from  
62 them i.e., underestimation of the horizontal wind (Hocking et al., 1990; Damle et al., 1994;  
63 Das et al., 2022). Thus, the study of the aspect of sensitivity of such VHF radars is of  
64 utmost importance given their use as powerful tools in deciphering winds and turbulence  
65 parameters from clear air and during disturbed conditions.

66 Earlier studies have shown that aspect sensitivity of backscatter echoes can be  
67 linked to the presence of a thin stable layer which is effectively a single sharp gradient in  
68 radio refractive index or to the presence of shear-generated steep layer structures  
69 (Hocking et al., 1986, 1990; Tsuda et al., 1997a, Das et al., 2008, 2022). A strong thermal  
70 gradient in the vicinity of tropical tropopause (16-18 km) acts like a perfect reflector  
71 causing high aspect sensitive VHF radar echoes (Jain et al., 1997; Das et al., 2008, 2016,  
72 2022). Quantitatively a rapid decrease of signal strength at an average of about 1.2 dB per  
73 degree till  $10^\circ$  tilt and at 0.6 dB per degree beyond that (Tsuda et al., 1997a; Anandan et  
74 al., 2008; Das et al., 2022) are attributed to Fresnel reflection/scattering and anisotropic  
75 turbulence up to  $10^\circ$  (Gage and Balsley, 1980) and those beyond  $10^\circ$  are attributed to

76 Bragg scale isotropic turbulent scattering (Rao et al., 1997) as observed for 49-53 MHz  
77 VHF radars. While previous studies focused mostly only on the orthogonal north-south,  
78 east-west variation of the echo strength (Damle et al., 1994; Jain et al., 1997; Qing et al.,  
79 2018; Ghosh et al., 2004; Das et al., 2008, 2016) due to the limitation of experiments,  
80 others have found an azimuthal dependence too (Tsuda et al., 1997b; Worthington et al.,  
81 1999; Das et al., 2022). The angular variation of the echo strength has been attributed to  
82 either diffuse reflection from stable temperature sheet structure or the presence of  
83 corrugated sheets or anisotropic turbulence (Das et al., 2014). Azimuth angle variation  
84 has been attributed to the presence of tilting layers which are generated due to gravity  
85 waves (Tsuda et al., 1997b; Rao et al., 2008) or mountain waves (Worthington 1999).  
86 Studies in these tilting layers have found small-scale Kelvin-Helmholtz instability (KHI)  
87 to be responsible for the redistribution of scatterers into a tilted layer (Worthington et  
88 al., 1997; Ghosh et al., 2004; Das et al., 2008, 2016). Primarily KHI is found to be in cores  
89 of large wind shears like above and below the jet stream or is created due to inertia  
90 gravity waves (IGW). Studies have found that in the UTL region, only a minimal amount  
91 of shear is needed to generate aspect-sensitive echoes (Ghosh et al., 2004). It has also  
92 been found that all zenith beam echo powers remain the same for well mixed i.e., isotropic  
93 turbulent layers. Previous volume imaging experiment of VHF aspect sensitive scatterers  
94 have shown tilted layers (Worthington, 2005). Thus, an understanding of the causative  
95 mechanisms for aspect sensitivity has been found in the above-mentioned atmospheric  
96 processes. But two salient points from the aforementioned studies are firstly that very  
97 few of these have been done to understand the total spatial dependence of aspect  
98 sensitivity i.e., both in the off-zenith and azimuthal directions mostly due to the limitation  
99 of radar scanning patterns and most of the studies have been performed in the higher and

100 mid-latitudes with only a handful of them being in the tropical low latitude belt, of which  
101 most are limited to the 53 MHz radar at Gadanki (Das et al., 2022).

102 In this study, a state-of-the-art, indigenously developed, and the world's first  
103 stratosphere-troposphere (ST) radar operating at 205 MHz at Cochin University of  
104 Science and Technology (CUSAT), Cochin (10.04°N, 76.33°E) (Samson et al., 2016;  
105 Mohanakumar et al., 2017) has been used. This radar has a 360-degree azimuthal beam  
106 steering capability which can provide full three-dimensional atmospheric dynamics and  
107 structure in both clear-air and in extreme weather conditions. There is no aspect  
108 sensitivity study so far using a 205 MHz atmospheric radar at any other place in the  
109 world. Here, the first results obtained from the experiments conducted during clear-air  
110 and disturbed weather conditions by operating CUSAT ST-Radar in multi-beam mode  
111 with azimuthal steering are presented. The experiments were designed by the optimum  
112 selection of zenith and azimuth beams, which will have a full-volume imaging scan within  
113 ~18 min. It is envisaged that the present experiment and results will have an important  
114 aspect in designing various experiments with CUSAT- ST radar, which is located at the  
115 gate-way of the Indian Summer Monsoon (ISM) region to better understand the  
116 dynamical processes taking place in the UTLS region in terms of radar scattering  
117 mechanism. Section 2 provides the experiment details with data analysis, background  
118 meteorological conditions in section 3, results and discussion in section 4 followed by  
119 concluding remarks in section 5.

## 120 **2. Experiment and Data Analysis**

### 121 **2.1. CUSAT ST Radar**

122 The CUSAT ST radar is unique in the sense that it uses the 205 MHz VHF frequency.  
123 It is a pulsed coherent Doppler radar with peak power aperture product of about  $1.6 \times$   
124  $10^8 \text{ W m}^2$  and 619 element antenna active phased array arranged on a rooftop in a

125 circular array of about 27 m diameter with an inter element spacing of  $0.7 \lambda$ . The radar  
126 beam can tilt up to a maximum of  $30^\circ$  in the off-zenith direction and cover  $0^\circ$ - $360^\circ$  in the  
127 azimuthal direction with a step interval of  $1^\circ$  (Samson et al., 2016; Mohanakumar et al.,  
128 2017). Detailed radar specifications are listed in Table 1.

129 The experiments were performed on July 21 and 22, 2022, which is in the active  
130 phase of the Indian Summer Monsoon (ISM) season. The Radar has been operated in four  
131 modes: viz. mode-1, mode-2, mode-3, and mode-4. Here mode-1 is the 5-beam  
132 configuration operation that is used to derive the wind components from the radar, and  
133 mode-2 is the continuous vertical observation. Mode-3 is the multibeam mode operated  
134 to study the orthogonal characteristics in the east-west and north-south directions with  
135 61 beams up to  $30^\circ$  angle in steps of  $2^\circ$ . Mode-4 is the volume scan mode using 31 beams  
136 in a scan cycle time of about 18 minutes, where the zenith and azimuthal variations are  
137 studied. Details of beam configuration and scans are given in Table 2 and the  
138 corresponding beam configuration in space for modes 1,2, 3, and 4 are shown in Figure  
139 1. The radar data is recorded in terms of I (in-phase) and Q (quadrature) values for each  
140 beam position of the scan which is processed by algorithms to read these values from the  
141 raw binary format file to produce the power spectrum and this has been utilized to derive  
142 the moments that have been essentially used in this work to further derive the wind and  
143 turbulence parameters using a multibeam technique to minimize errors.

## 144 **2.2. Radiosonde**

145 Regular GPS-based radiosonde (Chang Feng CF-06-A make) are launched at India  
146 Meteorological Department (IMD) from Cochin and Thiruvananthapuram ( $8.48^\circ\text{N}$ ,  
147  $76.95^\circ\text{E}$ ) at 05:30 and 17:30 LT. But on the day of experiment, we have radiosonde  
148 observation from Thiruvananthapuram only. These radiosondes have an accuracy of  
149 better than  $2 \text{ ms}^{-1}$  in wind velocity. The profiles obtained from radiosonde

150 measurements are interpolated into 100 m resolution. The soundings were obtained  
151 from the University of Wyoming sounding data archive  
152 (<http://weather.uwyo.edu/upperair/sounding.html>).

### 153 **2.3. Satellite observations**

154 The Constellation Observing System for Meteorology, Ionosphere, and Climate-2  
155 (COSMIC-2) satellite constellation gives excellent profiles of the atmosphere temperature  
156 and humidity by using the GPS Radio Occultation (RO) technique and has very good  
157 temporal and spatial coverage over the tropical region (Veenus et al., 2022). The absolute  
158 temperature difference between COSMIC-2 measured temperature with radiosonde  
159 observation is about 0.5 K and a standard deviation difference of 1.5 K. Hence the closest  
160 temporal and spatial occulted temperature profile obtained from COSMIC-2 has been  
161 utilized in the present study. In addition, the outgoing long-wave radiation (OLR)  
162 obtained from the imager aboard the geostationary Indian meteorological satellite  
163 (INSAT)-3DR, gives an indicator of intensity of convection.

### 164 **2.3. IMDAA reanalysis**

165 The Indian Monsoon Data Assimilation and Analysis (IMDAA) reanalysis is a high-  
166 resolution reanalysis data over the Indian Summer Monsoon (ISM) region developed by  
167 the Ministry of Earth Sciences (MoES), Government of India with the collaboration of Met  
168 Office, UK under the Indian Monsoon Mission project (Ashrit et al., 2020; Rani et al.,  
169 2021). The data assimilation scheme in IMDAA reanalysis used is 4D-Var (four-  
170 dimensional variational) of the upper-air atmospheric state and has assimilated both  
171 satellite and in situ observations and it's a unified model. The horizontal grid resolution  
172 is ~12 km and it has 63 vertical levels up to 40 km. Details can be found elsewhere (Ashrit  
173 et al., 2020; Rani et al., 2021). We also used winds and mean sea level pressure from  
174 IMDAA reanalysis.

### 175 **3. Meteorological background**

176           The experiments were conducted during the active phase of tropical easterly jet  
177 (TEJ). Figure 2 (a) shows the intensity of wind speed and direction at 100 hPa at 13:30  
178 LT on July 21 and 22, 2022. Wind speed and direction are obtained from IMDAA  
179 reanalysis. It is clear from the figure that the core of TEJ is located over the radar  
180 observational site. There is a variation of the core size and shape from July 21 to 22, 2022.  
181 As outgoing-long wave radiation (OLR) is considered as the proxy of convection, thus we  
182 have plotted OLR obtained from INSAT-3DR on both the days as shown in Figure 2 (b).  
183 On July 21, 2022, a clear sky is observed over the radar site, however, intense clouds were  
184 observed over the north Indian Ocean. In contradictory, we observed clouds on July 22,  
185 2022 over the radar site as well as over the central India and North Bay of Bengal. As such  
186 no low pressure systems were observed on both days (Figure 2 b).

### 187 **4 Results and Discussion**

#### 188 **4.1 Fan Sector and Volume scan**

189           Figure 3a shows the fan sector variation of signal-to-noise ratio (SNR) in East-  
190 West (EW) and North-South (NS) extending to a horizontal maximum of about 10 km on  
191 either side of the zenith beam using mode-3 experiment at 13:30 LT on July 22, 2022.  
192 Enhancement of the SNR across the horizontal direction at ~17 km in both the EW and  
193 NS fan sectors is seen in the vicinity of tropopause (VOT). Aspect-sensitive characteristics  
194 are clearly evident above ~12 km in both the SNR plots and it is observed that SNR  
195 decreases with an increase in off-zenith angles. A similar variation of SNR has earlier been  
196 reported in those height ranges for the 53 MHz Gadanki MST radar (Jain et al., 1997;  
197 Ghosh et al., 2004; Das et al., 2008, 2016) during both clear and disturbed weather  
198 conditions. Similarly, a fan sector study of the beam line-of-sight Doppler velocity gives  
199 an idea about the dynamics as seen in Figure 3b where a stark difference is noted in the

200 strength and characteristics of the Doppler values from EW and NS fan sectors. The strong  
201 easterly Doppler was observed as a Tropical Easterly Jet (TEJ) above 12 km which is a  
202 feature related to the ISM. On the contrary, the NS Doppler has asymmetric features  
203 although not as strong as the EW Doppler. Figure 3c shows the fan sector map of the  
204 uncorrected half-power full spectral width which is quite similar in feature to the SNR.  
205 Enhancements in spectral width corresponding to areas of enhanced SNR are observed,  
206 which indicates the presence of turbulence. This spectral width can be contaminated with  
207 non-turbulent factors like broadening due to the finite volume of the beam, shear  
208 broadening, and transient effects, which will be discussed later. Similar features can also  
209 be noted for July 21, 2022 as shown in supplementary Figure S1.

210 Figure 4 shows the SNR variation with zenith angles up to  $30^\circ$  in the EW and NS  
211 planes for different heights during mode-3 experiment on July 22, 2022. It can be seen at  
212 11.4 km that the SNR falls very gradually with increasing off-zenith angle remaining  
213 almost same up to  $\sim 6^\circ$  on either side of the zenith beam in both EW and NS directions  
214 showing isotropy in that region. Similar feature can be noted for 12.4 km too but only in  
215 the EW direction as NS plane shows regularly decreasing SNR feature with increasing off-  
216 zenith angle. Such EW and NS plane asymmetry is noted at 14 km and 16.4 km too as  
217 shown along with significant off-zenith enhancement of SNR which can be attributed to  
218 tilted scatterer layer perpendicular to the beam direction (Muschinski and Wode, 1998).  
219 For July 21, 2022 such variation of SNR is also observed with similar EW and NS  
220 asymmetry as shown in Figure S2.

221 After averaging all fan scans for both EW and NS directions respectively heights  
222 with least isotropy, off-zenith asymmetry and off-zenith enhancement are found out.  
223 From such heights with progressively decaying signal, it is estimated that the signal  
224 strength decreases by 0.75 dB per degree from 0 to 10 degree off-zenith, 0.9 dB per

225 degree from 10 to 20 degree off-zenith and 0.3 dB per degree beyond 20 degree off-zenith  
226 using the formula:

$$227 \quad Decay = \frac{SNR_{\theta_a} - SNR_{\theta_b}}{\theta_a - \theta_b} \quad (1)$$

228 where  $\theta_a$  takes values  $0^\circ, 10^\circ, 20^\circ$  and  $\theta_b$  takes values  $10^\circ, 20^\circ, 30^\circ$  respectively.

229 It is observed from Figure 5 that Doppler frequency spectra as a function of zenith  
230 angle for both EW and NS plane scans are mostly narrow for both the panels especially  
231 for lesser zenith angles, showing smaller spectral widths between 13:01:36-14:46:00 LT  
232 on July 22, 2022. The slope of the mean spectra indicates and validates the presence of  
233 background wind in both the orthogonal planes, a feature previously observed by Das et  
234 al. (2008) for a different location. Notably, much higher range of Doppler values are seen  
235 in EW panel owing to the strong Doppler associated with the TEJ as shown earlier.  
236 Weaker echoes for higher Doppler values at large zenith angles are consistent with the  
237 fan sector plot for the same. Further Figure S3 shows almost exactly the same features  
238 on July 21, 2022 during the time span.

239 Figure 6 shows the slice maps of the radar scan volume which provide the spatial  
240 variation of SNR, Doppler, and spectral width at different height levels at 12 LT on July  
241 22, 2022. It is to be noted that above 14 km the SNR shows a general aspect sensitivity  
242 with echo strengths decreasing towards the edge of the volume slices but with a very  
243 evident asymmetry in the azimuthal direction for all three heights. Isotropic scattering is  
244 observed at  $\sim 17.6$  km, which is the tropopause level as observed from the temperature  
245 profile. In the VOT level, the volume slice shows very regular high SNR spread around the  
246 zenith region signifying a stratified layer. While much stronger asymmetry of signal is  
247 noted at 14 km with strong off-zenith enhancement. This feature as explained earlier may  
248 be attributed to the presence of tilting layers. Symmetric Doppler feature is observed in

249 Figure 6b. The spectral width slice maps shown in Figure 6c represent the spatial  
 250 distribution of turbulence. Volume slices for July 21, 2022 are shown in Figure S4.

## 251 **4.2 Aspect sensitivity mechanisms and characteristics**

252 Aspect sensitivity as mentioned before can be understood by the relative strength  
 253 of the zenith beam echo with respect to the off-zenith echoes as shown in Figure 7. It can  
 254 clearly be seen that the deviation of SNR from the zenith value is more prevalent above  
 255 the heights of  $\sim 12$  km for the angles shown for east, west, north, and south directions. In  
 256 all the directions, a decrease in the difference below zero in between 14-16 km heights  
 257 and an increasing trend above 16 km for higher off-zenith angles is observed. From such  
 258 distribution of SNR, it can be said that for layers below 10-12 km, the echo strengths are  
 259 more or less the same for most off-zenith angles due to isotropic turbulent scatter. While  
 260 a positive zenith-off-zenith SNR difference can be attributed to the presence of stratified  
 261 layer, a negative difference for the same as noted between  $\sim 14$ -15 km can possibly be  
 262 due to the tilting layers associated with gravity waves or KHI, which will be discussed.  
 263 Figure S5 shows similar features but for July 21, 2022.

264 Aspect sensitivity parameters can be characterized by the aspect angle ( $\theta_s$ ) which  
 265 is the measure of anisotropy and can be derived from the backscatter echo powers for  
 266 one zenith angle with respect to another (Hocking 1986; Hocking 1989) as shown in  
 267 equation (2):

$$268 \quad \theta_s = \sin^{-1} \sqrt{\frac{\sin^2 \theta_{b_2} - \sin^2 \theta_{b_1}}{\ln\left(\frac{P(\theta_{b_1})}{P(\theta_{b_2})}\right)} - \sin^2 \theta_0} \quad (2)$$

269 where  $\theta_0 (= \theta_{3 \text{ dB}} / \sqrt{\ln 2})$ , the  $e^{-1}$  half-width of the radar polar diagram, is  $1.8^\circ$  for a  $\theta_{3 \text{ dB}}$   
 270 (3-dB beam width) of  $3^\circ$  in the CUSAT ST radar.  $\theta_b$  is the zenith or beam pointing angle.  
 271 Aspect angle is calculated with respect to the zenith beam here thus,  $\theta_{b_1} = 0^\circ$ . Another  
 272 parameter is the corresponding horizontal correlation length ( $\zeta$ ) (length-to-depth ratio)

273 of the scatterers in the atmosphere which is obtained (Hocking et al 1990) by equation  
274 (3):

$$275 \quad \zeta = \frac{15.2\lambda}{\theta_s} \quad (3)$$

276 Corresponding values of  $\theta_s$  and  $\zeta$  for different off-zenith beam angles with respect to the  
277 zenith beam for all the four orthogonal directions *viz.*, east, west, north, and south on July  
278 22, 2022 as shown in Figure 8. To understand the significance of Fresnel scattering/  
279 reflection the condition  $\zeta \geq 0.29D$  ( $D$  is diameter of the antenna) (Gage 1990) must hold.  
280 In this case accounting for the geometry of the radar  $\zeta \geq 7.187$  m and correspondingly  
281  $\theta_s \leq 3.093^\circ$  give the Fresnel scattering threshold. Figure 8 shows lower values of aspect  
282 angle for lesser zenith angles and corresponding higher correlation length above 14 km  
283 height for all four directions (E,W,N,S) with slight variations. This implies the presence of  
284 anisotropic scattering mechanisms such as Fresnel scattering or anisotropic turbulence.  
285 Values of  $\theta_s$  and  $\zeta$  occurring below and above the thresholds marked respectively are seen  
286 only in layers between 12-17 km, signifying Fresnel scattering/reflection. Some  
287 differences in pattern in the EW and NS directions especially in the lower heights below  
288 12 km show the azimuthal asymmetry of aspect sensitivity. Similar distribution of aspect  
289 angle and correlation length on July 21, 2022 can be seen in Figure S6.

290 The anisotropy estimated above affects the actual beam pointing angle at different  
291 heights, but from the measure of  $\theta_s$  the effective beam pointing angle can be calculated  
292 as:

$$293 \quad \sin(\theta_{eff}) = \sin(\theta_b) \left(1 + \frac{\sin^2\theta_b}{\sin^2\theta_s}\right)^{-1} \quad (4)$$

294 This is the source of underestimation of winds using the radar. Figure 9 shows the  
295 effective beam pointing angle for zenith angles up to  $16^\circ$  on July 22, 2022. Deviation from  
296 the original beam pointing angle is clearly visible above 12 km with very large deviation

297 at and above 14 km up to ~16 km height for all zenith beam in all the four orthogonal  
 298 directions. Interestingly, it is to be noted that for angles less than 6° the deviation from  
 299 the true pointing angle is more as compared to angles above 6°, this leads to the  
 300 significant underestimation of wind when using such low zenith angles. Almost same  
 301 trend is also observed for July 21, 2022 as shown in Figure S7 but with significantly higher  
 302 deviations for lower angles up to 8°. Thus, knowing the effective beam pointing angle  
 303 leads to a quantitative measure of the underestimation of wind components at different  
 304 heights.

### 305 **4.3 Dependency of aspect sensitivity on wind shear and atmospheric stability**

306 Both the atmospheric stability and vertical shear play a major role in the aspect  
 307 sensitivity of VHF radar (e.g., Ghosh et al., 2004; Das et al., 2022). Thus, we estimate the  
 308 atmospheric stability ( $N^2$ ) using equation (5):

$$309 \quad N^2 = \frac{g}{\theta} \left( \frac{\partial \theta}{\partial z} \right) \quad (5)$$

310 where,  $N$  is the Brunt-Vaisala frequency,  $\theta$  the potential temperature, which is estimated  
 311 from the temperature profile obtained from COSMIC-2 GPS RO. Further, vertical shear of  
 312 horizontal wind ( $S^2$ ) is estimated using equation (6):

$$313 \quad S^2 = \left( \frac{\partial u}{\partial z} \right)^2 + \left( \frac{\partial v}{\partial z} \right)^2 \quad (6)$$

314 Where,  $u$  and  $v$  are the CUSAT ST radar derived velocity of zonal and meridional wind,  
 315 respectively. Figure 10 shows a variation of difference of SNR with respect to the zenith  
 316 beam with square of (a) wind shear (b) stability parameters for July 22, 2022. It is clearly  
 317 evident from both the top (EW) and bottom (NS) panels of Figure 10a that the probability  
 318 of having high aspect sensitivity is enhanced when  $S^2$  is less than  $0.25 \times 10^{-3} \text{ s}^{-2}$ , shown as  
 319 a denser cluster of points. Beyond this threshold it can be said that the increased shear  
 320 causes turbulent mixing resulting in isotropy of the scatterers. Shear also does play an

321 important role of resharpener of refractive index gradient as pointed out and explained  
322 by Muschinski and Wode (1998). Similarly in Figure 10b for the case of  $N^2$  the same  
323 characteristics can be seen where with a dense cluster of points inside the  $0.25 \times 10^{-3} \text{ s}^{-2}$   
324 threshold limit albeit not as strongly defined as the shear parameter. But it can be  
325 concluded that beyond the stability threshold the scatterers become isotropic. The exact  
326 same feature is also reproduced for July 21, 2022 as seen in Figure S8. Previous study by  
327 Das et al. (2022) showed similar results for the Gadanki MST radar at 53 MHz.

### 328 **4.3 Role of Kelvin-Helmholtz Instability and gravity waves in tilting layer**

329 The preceding analyses throw light on the spatial aspect sensitivity characteristics  
330 but to understand the temporal evolution of the backscatter echoes, the CUSAT ST radar  
331 was operated in mode-2, i.e., continuous vertical observations made from 14:10 to 16:10  
332 LT on July 22, 2022. Figure 11 shows the height-time-intensity (HTI) plots of (a) SNR, (b)  
333 vertical velocity, and (c) half-power full spectral width. Enhanced SNR layer is seen in the  
334 VOT similar to the fan sector plots in Figure 11a. Aspect sensitivity is very clearly  
335 observed around and above 12 km. An enhanced SNR structure is seen at around 14 km  
336 height with a descending trend with time from 15:30 LT onwards. The corresponding HTI  
337 plot of vertical velocity in Figure 11b obtained from the line-of-sight Doppler ( $w =$   
338  $-\lambda/2 d$ ) shows alternating upward and downward velocities at  $\sim 14$  km after 15:30 LT.  
339 This resembles a turning structure which can be attributed to KHI. Such a pronounced  
340 alternating episode of updraft and downdraft is not seen anywhere else in the HTI plot  
341 but a feature of note is the presence of strong updrafts above 14 km height for the given  
342 time period owing to the convective conditions on the day most notably above the KHI  
343 structure in the VOT. Strong descending downdraft structures are seen below 10 km after  
344 the strong KHI signature. In Figure 11c uncorrected half power full spectral width shows  
345 enhanced turbulence corresponding to high spectral width mostly below 12 km height

346 temporally corresponding to the KHI and the descending downdraft structure.  
347 Enhancement of spectral width can be seen just below the tropopause all through and  
348 around 14 km height post 15:30 LT matching with the SNR feature in Figure 11a. The  
349 observed features mentioned above are quantified by studying the stability, wind shear,  
350 as shown in Figure 12 for July 22, 2022. COSMIC-2 temperature profile and wind speed  
351 components obtained from the radar. It has been found that the cold point tropopause  
352 (CPT) lies at about 17.6 km for this time of observation and a huge increase in the stability  
353 and decrease in wind shear at that level is seen in Figures 12c and 12d. Comparing all the  
354 heights it can be said from previous studies (Ghosh et al., 2004) that a sharp gradient  
355 instability and reduction of wind shear indicates aspect sensitivity thus showing that  
356 aspect sensitivity is dependent on the thermal structure of the atmosphere. Figure 12e  
357 shows the corresponding Richardson Number ( $Ri=N^2/S^2$ ) profile which gives a measure  
358 of turbulence. Values less than 1 suggest turbulent layers and more than 1 suggest aspect-  
359 sensitive regions. A sharp reduction in Richardson number to under the threshold value  
360 at around 14 km explains the turbulent feature observed in Figure 11. While aspect  
361 sensitive layers do not occur much up to 10 km as observed, these become more  
362 prevalent above 12 km height except for the height range of around 16 km. This height  
363 range corresponds to the TEJ core as seen in Figure 12a and this feature also matches  
364 with the wind profile derived from radiosonde observation for the day. The tropopause  
365 being a stably stratified layer shows maximum stability, minimum shear, and an  
366 extremely high value of Richardson number, indicating the presence of KHI. Similar  
367 features are noted for July 21, 2022 as shown in Figure S9.

368         The asymmetry in SNR (Fig.7 and Fig. S5) can be due to this observed KHI,  
369 however gravity waves can also contribute for titling layer. To get further insight, the  
370 time-series of vertical velocity is subjected to Fast-Fourier transform (FFT) to obtain the

371 gravity wave spectra. Figure 13 shows the (a) power spectra of vertical velocity at 14.8  
372 and 15.7 km. The dominant period of gravity waves observed are 10-12 min and 16-18  
373 min from the power spectra during 14:10-17:30 LT on July 22, 2022. Thus, the height  
374 profiles for corresponding dominant periods are extracted and shown in Fig. 13 (b) and  
375 (c). Left panels show the amplitude and right panel shows the phase. The maximum  
376 amplitudes are observed at 14-16 km for 10-12 min waves, whereas it is at 16-18 km for  
377 16-18 min waves. This indicates there are two sources for these polychromatic waves.  
378 The typical property of any atmospheric wave is the propagation of its phase and energy  
379 in space and time. The energy will propagate upwards and the phase will propagates  
380 downwards, which is clearly observed in the phase profiles of both the waves. These  
381 waves can in principle modulate the horizontal stratified layer to form tilting layer as  
382 suggested in the earlier studies (e.g. Tsuda et al., 1997b; Muschinski and Wode, 1998; Rao  
383 et al., 2008)

#### 384 **4.4 Corrections for non-turbulent factor of spectral width**

385 The observed spectral width is actually a combination of both turbulent and non-  
386 turbulent contributions as mentioned above. Thus, it is important to understand and  
387 quantify the contribution due to non-turbulent factors such as beam-broadening, wind  
388 shear, other transient effects and gravity waves. Although the effect of beam-broadening  
389 and wind shear have been studied separately it has been seen that simply adding them  
390 up from a 1D model case is not sufficient for actual 2D/3D cases (Nastrom, 1997). The  
391 simple yet effective model developed by Nastrom (1997) under very ideal assumptions  
392 such as constant wind speed and wind shear under 2D model actually deviate from the  
393 real radar case. This has been addressed by the model proposed by Deghghan and  
394 Hocking (2011) for a 3D case (D-H model) with some more modifications to fit real wind  
395 profile which encapsulates the singular contribution due to the two factors and their

396 combined effect as well. This has been successfully used in studies related to real radars  
 397 (e.g., Chen et al. 2022). Ignoring transient and gravity wave related broadening effects  
 398 due to their diminutive contributions with respect to the other factors, the observed  
 399 spectral width can be defined as:

$$400 \quad \sigma_o^2 = \sigma_t^2 + \sigma_{s\&b}^2 \quad (7)$$

401 Where  $\sigma_t^2$  is the turbulent part and  $\sigma_{s\&b}^2$  the contribution due to shear and beam  
 402 broadening is given by the D-H model as:

$$403 \quad \sigma_{s\&b}^2 = \frac{\theta^2}{k} v^2 \cos^2 \chi - a_0 \frac{\theta}{k} \sin \chi \left( v \frac{\partial v}{\partial z} \zeta \right) + b_0 \frac{2 \sin^2 \chi}{8k} \left( \frac{\partial v}{\partial z} \zeta \right)^2 + c_0 (\cos^2 \chi \sin^2 \chi) |v \xi| +$$

$$404 \quad d_0 (\cos^2 \chi \sin^2 \chi) \xi^2 \quad (8)$$

405 Where  $k = 4 \ln 2$ ,  $\zeta = 2r\theta \sin \chi$ ,  $\xi = \frac{\partial v}{\partial z} \frac{\Delta r}{\sqrt{12}}$ ,  $a_0 = 0.945$ ,  $b_0 = 1.500$ ,  $c_0 = 0.030$ ,  $d_0 = 0.825$   
 406 and  $\theta$  is the half power half width,  $v$  is the horizontal wind speed,  $\chi$  is the zenith angle,  $\frac{\partial v}{\partial z}$   
 407 is the vertical shear of horizontal wind,  $r$  is the distance from the radar and  $\Delta r$  is the  
 408 range resolution which is 180 m in the present experiment.

409 Figure 14 shows the (a) wind speed, (b) vertical shear of horizontal winds, observed half-  
 410 power full spectral width for (c) zenith, and (d) 12 degree off-zenith (East, West, North  
 411 and South) along with theoretical estimation from D-H model, respectively. This is the  
 412 case where high wind speed (as high as  $> 45 \text{ ms}^{-1}$ ) (Fig. 14 a) and strong wind shear (Fig.  
 413 14 b) are observed in the UTLS region. The observed turbulence (uncorrected) (Fig. 12 c,  
 414 d) needs to be corrected for beam broadening for vertical beam and both beam and shear  
 415 broadening for off-zenith beams. Thus, using D-H model, we estimated the profile for  
 416 these non-turbulent factors as shown in Fig. 14 (c) and (d) (black square). The model  
 417 spectral width profiles (non-turbulent factors) above 14 km is exceeding then observed  
 418 spectral width, thus the effective spectral width will be negative. Although such negative  
 419 values should not exist theoretically, practically their presence and implication of

420 'negative' energy dissipation rates is addressed by previous studies (Deghghan and  
421 Hocking, 2011; Chen et al. 2022). The main reasons for such negative spectral width after  
422 correction by non-turbulent factors is due to high wind speed and strong shear  
423 contributions. A separate study is planned in near future to address these issue.

#### 424 **4.6 Underestimation of horizontal winds due to aspect sensitivity**

425 One of the consequences of high aspect sensitivity is the underestimation of  
426 horizontal winds. The lower the effective beam pointing angle due to high aspect  
427 sensitivity, higher will be the underestimation of the horizontal wind. This is quantified  
428 by the factor R defined as equation (7) :

$$429 \quad R = 1 + \frac{\sin^2 \theta_0}{\sin^2 \theta_S} \quad (7)$$

430 The percentage underestimation of horizontal wind given in Fig.15 shows that larger  
431 underestimation is observed for layers with higher aspect sensitivity. It can also be seen  
432 that the highest underestimation comes for lesser angles such as 6°, 8° with the  
433 percentage going as high as 20% or more. While for angles  $\geq 10^\circ$  the underestimation falls  
434 to less than 10% for July 22, 2022 and similar results are also seen for July 21, 2022 as  
435 shown in Figure S10. Previous studies for 53 MHz radar at Gadanki have also shown  
436 similar results (Jain et al., 1997; Das et al., 2022). Thus, it is necessary to correct the  
437 horizontal wind velocities by taking aspect sensitivity into consideration to get correct  
438 information regarding the prevalent winds.

#### 439 **5. Concluding remarks**

440 In the present study, aspects sensitivity characteristics for CUSAT ST-radar  
441 operating at 205 MHz are assessed for the first time. An experiment was designed to  
442 obtain the full volume imaging of the radar backscattering echoes to show the presence  
443 of anisotropic and isotropic layers during the Indian summer monsoon. The present

444 study revealed that the volume scanning of the radar can provide a better understanding  
445 of the underlying plausible mechanisms for the occurrence of turbulence, and aspect  
446 sensitivity characteristics. Different parameters associated with aspect sensitivity  
447 characteristics are also estimated from the CUSAT ST-radar. Aspect sensitivity is found to  
448 be present in layers mostly above 12 km height up to the tropopause level which was well  
449 detected as a stable stratified layer from the analysis of SNR, spectral width, and  
450 Richardson number. The important role that atmospheric stability and wind shear can  
451 play in generating anisotropic scattering for aspect sensitive signals is highlighted in the  
452 present analyses. The possible presence of tilting layers can be inferred from the strong  
453 off zenith enhancement of SNR which can be attributed to possible Kelvin-Helmholtz  
454 instability occurring in the height of about 14 km as well as polychromatic gravity waves  
455 which can be confirmed from continuous zenith observations. High aspect sensitivity is  
456 observed in the vicinity of tropopause and other stratified stable layers, resulting in the  
457 underestimation of horizontal winds.

458

#### 459 **Acknowledgements**

460 The authors are greatly appreciative to the technical and scientific teams of ACARR-  
461 CUSAT, Cochin for conducting the experiment and providing the radar data used in this  
462 study. The authors also thank the teams of the Ministry of Earth Science (IMD &  
463 NCMRWF), UK Met-Office and COSMIC for providing the data used in the study. Authors  
464 NP and VV thank the Indian Space Research Organisation (ISRO) for providing a research  
465 fellowship during the study period.

#### 466 **Conflict of Interest**

467 The authors declare no conflicts of interest relevant to this study.

#### 468 **Data Availability Statement**

469 The CUSAT ST radar data used for the present study can be downloaded from the website  
470 [https://spl.gov.in/SPL/images/CUSAT ST radar multibeam](https://spl.gov.in/SPL/images/CUSAT_ST_radar_multibeam). This is a compressed folder  
471 (.zip file), which contains all modes of radar data used in the study. Users are requested  
472 to obtain permission from Director, ACARR-CUSAT and authors for using the CUSAT ST  
473 radar data for any scientific studies. COSMIC-2, radiosonde, IMDAA reanalysis data are  
474 publicly available datasets. COSMIC-2 data is available in the website  
475 <https://data.cosmic.ucar.edu/gnss-ro/cosmic2/nrt/level2>. Radiosonde data are  
476 available from the University of Wyoming sounding data archive  
477 <http://weather.uwyo.edu/upperair/sounding.html>. IMDAA reanalysis data can be  
478 downloaded from <https://rds.ncmrwf.gov.in/> upon registration.

479

## 480 **References**

- 481 Anandan, V. K., Rao, I. S., & Reddy, P. N. (2008). A study on optimum tilt angle for wind  
482 estimation using Indian MST radar. *Journal of Atmospheric and Oceanic*  
483 *Technology*, 25(9), 1579-1589. doi: 10.1175/2008JTECHA1030.1.
- 484 Ashrit, R., Rani, S.I., Kumar, S., Karunasagar, S., Arulalan, T., Francis, T., Routray, A., Laskar,  
485 S.I., Mahmood, S., Jerney, P., Maycock, A., Renshaw, R., George, J.P., Rajagopal, E.N.  
486 (2020). IMDAA regional reanalysis: performance evaluation during  
487 Indian summer monsoon season. *Journal of Geophysical Research-Atmosphere*, 125 (2),  
488 e2019JD030973 <https://doi.org/10.1029/2019JD030973>.
- 489 Chen, Z., Tian, Y., & Lü, D. (2022). Turbulence Parameters in the Troposphere—Lower  
490 Stratosphere Observed by Beijing MST Radar. *Remote Sensing*, 14(4), 947.  
491 <https://doi.org/10.3390/rs14040947>
- 492 Damle, S. H., Chakravarty, T., Kulkarni, A., & Balamuralidhar, P. (1994). Aspect sensitivity  
493 measurements of backscatter with ST mode of the Indian MST radar. *Indian Journal of*

494 *Radio and Space Physics*, 23, 67–70.  
495 <https://nopr.niscpr.res.in/handle/123456789/35844>.

496 Das, S. S., Patra, A. K., & Narayana Rao, D. (2008). VHF radar echoes in the vicinity of  
497 tropopause during the passage of tropical cyclone: First observations from the  
498 Gadanki MST radar. *Journal of Geophysical Research: Atmospheres*, 113(D9). doi:  
499 10.1029/2007JD009014.

500 Das, S. S., K. K. Kumar, K. N. Uma, M. V. Ratnam, A. K. Patra, S. K. Das, A. K. Ghosh, et al.  
501 (2014). Modulation of Thermal Structure in the Upper Troposphere and Lower  
502 Stratosphere (UTLS) Region by Inertia Gravity Waves: A Case Study Inferred from  
503 Simultaneous MST Radar and GPS Sonde Observations. *Indian Journal of Radio and*  
504 *Space Physics* 43 (1), 11–23. <http://nopr.niscair.res.in/handle/123456789/27168> .

505 Das, S. S., Venkat Ratnam, M., Uma, K. N., Patra, A. K., Subrahmanyam, K. V., Girach, I. A.,  
506 Suneeth, K. V., et al. (2016). Stratospheric intrusion into the troposphere during the  
507 tropical cyclone Nilam (2012). *Quarterly Journal of the Royal Meteorological*  
508 *Society*, 142(698), 2168-2179. doi: 10.1002/qj.2810.

509 Das, S. S., Ratnam, M. V., Rao, M. D., & Uma, K. N. (2022). Volume imaging of aspect  
510 sensitivity in VHF radar backscatters: first results inferred from the Advanced Indian  
511 MST radar (AIR). *International Journal of Remote Sensing*, 43(12), 4517-4540. doi:  
512 10.1080/01431161.2022.2111667.

513 Dehghan, A., & Hocking, W. K. (2011). Instrumental errors in spectral-width turbulence  
514 measurements by radars. *Journal of atmospheric and solar-terrestrial physics*, 73(9),  
515 1052-1068. <https://doi.org/10.1016/j.jastp.2010.11.011>

516 Gage, K. S. (1990). Radar observations of the free atmosphere: Structure and dynamics.  
517 In *Radar in Meteorology: Battan Memorial and 40th Anniversary Radar Meteorology*

518 *Conference*, 534-565. Boston, MA: American Meteorological Society. doi:10.1007/978-  
519 1-935704-15-7\_37

520 Gage, K. S., & Balsley, B. B. (1980). On the scattering and reflection mechanisms  
521 contributing to clear air radar echoes from the troposphere, stratosphere, and  
522 mesosphere. *Radio Science*, 15(2), 243-257. doi: 10.1029/RS015i002p00243.

523 Ghosh, A. K., Das, S. S., Patra, A. K., Rao, D. N., & Jain, A. R. (2004). Aspect sensitivity in the  
524 VHF radar backscatters studied using simultaneous observations of Gadanki MST  
525 radar and GPS sonde. *Annales Geophysicae*, 22(11),4013-4023. Göttingen, Germany:  
526 Copernicus Publications. doi: 10.5194/angeo-22-4013-2004.

527 Hocking, W. K. (1985). Measurement of turbulent energy dissipation rates in the middle  
528 atmosphere by radar techniques: A review. *Radio Science*, 20(6), 1403-1422.  
529 doi:10.1029/RS020i006p01403

530 Hocking, W. K. (1989). "Target Parameter Estimation." In *MAP Handbook*, edited by S.  
531 Fukao, 228-268. Vol. 30. SCOSTEP Secr., Univ of Ill. *Urbana*.

532 Hocking, W. K., Rüster, R., & Czechowsky, P. (1986). Absolute reflectivities and aspect  
533 sensitivities of VHF radio wave scatterers measured with the SOUSY radar. *Journal of*  
534 *atmospheric and terrestrial physics*, 48(2), 131-144, doi:10.1016/0021-  
535 9169(86)90077-2.

536 Hocking, W. K., Fukao, S., Tsuda, T., Yamamoto, M., Sato, T., & Kato, S. (1990). Aspect  
537 sensitivity of stratospheric VHF radio wave scatterers, particularly above 15-km  
538 altitude. *Radio Science*, 25(4), 613-627. doi: 10.1029/RS025i004p00613

539 Jain, A. R., Rao, Y. J., & Rao, P. B. (1997). Aspect sensitivity of the received radar backscatter  
540 at VHF: Preliminary observations using the Indian MST radar. *Radio Science*, 32(3),  
541 1249-1260. doi: 10.1029/97RS00252.

542 Mohanakumar, K., Kottayil, A., Anandan, V. K., Samson, T., Thomas, L., Satheesan, K,  
543 Rebello, R. et al. (2017). Technical details of a novel wind profiler radar at 205  
544 MHz. *Journal of Atmospheric and Oceanic Technology*, 34(12), 2659-2671. doi:  
545 10.1175/JTECH-D-17-0051.1.

546 Muschinski, A., & Wode, C. (1998). First in situ evidence for coexisting submeter  
547 temperature and humidity sheets in the lower free troposphere. *Journal of the*  
548 *Atmospheric Sciences*, 55(18), 2893-2906. doi:10.1175/1520 -  
549 0469(1998)055<2893:FISEFC>2.0.CO;2.

550 Nastrom, G. D. (1997). Doppler radar spectral width broadening due to beamwidth and  
551 wind shear. *Annales Geophysicae*, 15(6), 786-796. Springer-Verlag.  
552 <https://doi.org/10.1007/s00585-997-0786-7>

553 Qing, H., Zhao, Z., Xu, Y., & Zhou, C. (2018). Observation and study of the aspect sensitivity  
554 and echo mechanism based on the Wuhan MST radar. *IEEE Geoscience and Remote*  
555 *Sensing Letters*, 16(2), 211-215. doi:10.1109/LGRS.2018.2871824.

556 Rao, D. N., Kishore, P., Rao, T. N., Rao, S. V. B., Reddy, K. K., Yarraiah, M., & Hareesh, M.  
557 (1997). Studies on refractivity structure constant, eddy dissipation rate, and  
558 momentum flux at a tropical latitude. *Radio Science*, 32(4), 1375-1389. doi:  
559 10.1029/97RS00251.

560 Rao, T. N., Uma, K. N., Rao, D. N., & Fukao, S. (2008). Understanding the transportation  
561 process of tropospheric air entering the stratosphere from direct vertical air motion  
562 measurements over Gadanki and Kototabang. *Geophysical Research Letters*, 35(15).  
563 <https://doi.org/10.1029/2008GL034220>

564 Rani, S.I., Arulalan, T., George, J.P., Rajagopal, E.N., Renshaw, R., Maycock, A., Barker, D.M.,  
565 Rajeevan, M. (2021). IMDAA: high-resolution satellite-era reanalysis for the Indian

566 monsoon region. *Journal of Climate*. 34 (12), 5109–5133.  
567 <https://doi.org/10.1175/JCLI-D-20-0412.1>.

568 Röttger, J., & Liu, C. H. (1978). Partial reflection and scattering of VHF radar signals from  
569 the clear atmosphere. *Geophysical Research Letters*, 5(5), 357-360. doi:  
570 10.1029/GL005i005p00357.

571 Samson, T. K., Kottayil, A., Manoj, M. G., Babu, B., Rakesh, V., Rebello, R., et al. (2016).  
572 Technical aspects of 205 MHz VHF mini wind profiler radar for tropospheric probing.  
573 *IEEE Geoscience and Remote Sensing Letters*, 13(7), 1027–1031.  
574 <https://doi.org/10.1109/lgrs.2016.2561965>.

575 Tsuda, T., VanZandt, T. E., & Saito, H. (1997a). Zenith-angle dependence of VHF specular  
576 reflection echoes in the lower atmosphere. *Journal of Atmospheric and Solar-Terrestrial*  
577 *Physics*, 59(7), 761-775. doi: 10.1016/S1364-6826(96)00057-0.

578 Tsuda, T., Gordon, W. E., & Saito, H. (1997b). Azimuth angle variations of specular  
579 reflection echoes in the lower atmosphere observed with the MU radar. *Journal of*  
580 *Atmospheric and Solar-Terrestrial Physics*, 59(7), 777-784. doi: 10.1016/S1364-  
581 6826(96)00058-2.

582 Veenus, V., Das, S. S., Sama, B., and Uma, K. N. (2022), A comparison of temperature and  
583 relative humidity measurements derived from COSMIC-2 radio occultations with  
584 radiosonde observations made over the Asian summer monsoon region, *Remote*  
585 *Sensing Letters*, 13 (4), 394–405, doi:10.1080/2150704X.2022.2033345.

586 Worthington, R. M. (1999). Calculating the azimuth of mountain waves, using the effect of  
587 tilted fine-scale stable layers on VHF radar echoes. *Annales Geophysicae*, 17(2), 257-  
588 272. Göttingen, Germany: Springer Verlag. doi: 10.1007/s00585-999-0257-4.

589 Worthington, R. M. (2005). VHF volume-imaging radar observation of aspect-sensitive  
590 scatterers tilted in mountain waves above a convective boundary layer. In *Annales*  
591 *Geophysicae*, 23(4), 1139-1145. doi:10.5194/angeo-23-1139-2005.

592 Worthington, R. M., & Thomas, L. (1997). Long-period unstable gravity-waves and  
593 associated VHF radar echoes. *Annales Geophysicae*, 15(6), 813-822. Berlin/Heidelberg:  
594 Springer-Verlag. doi: 10.1007/s00585-997-0813-8.

595 Worthington, R. M., Palmer, R. D., & Fukao, S. (1999). An investigation of tilted aspect-  
596 sensitive scatterers in the lower atmosphere using the MU and Aberystwyth VHF  
597 radars. *Radio Science*, 34(2), 413-426. doi: 10.1029/1998RS900028.

598  
599

## 600 **Figure captions**

601 **Figure 1.** Beam configurations for different modes of experiment. See Table 2 for details.

602 **Figure 2.** (a) Wind speed and direction (arrow) at 100 hPa, and (b) outgoing-long wave  
603 radiation along with mean sea level pressure at 13:30 LT on July 21 (left) and 22 (right),  
604 2022. CUSAT ST radar is marked in each panels.

605 **Figure 3.** Fan sector maps in the E-W and N-S directions for (a) Signal-to-Noise (SNR),  
606 (b) Doppler velocity values, (c) uncorrected observed half-power full Spectral width at  
607 13:30 LT on July 22, 2022.

608 **Figure 4.** SNR as a function of zenith angles up to 30° in East-West (left) and North-South  
609 (right) directions for heights of 11.4 km, 12.4 km, 14 km and 16.4 km for July 22, 2022

610 **Figure 5.** Doppler spectra as a function of zenith angle for July 22, 2022 for East-West  
611 (left) and North-South (right) planes.

612 **Figure 6.** Volume scan slices at 14 km, 16 km and 17.6 km for (a) SNR, (b) Doppler, (c)  
613 uncorrected half-power full spectral width at 12 LT on July 22, 2022.

614 **Figure 7.** Altitude profiles of SNR difference between zenith and a few off-zenith angles  
615 for East, West, North, and South directions.

616 **Figure 8.** Aspect Angle  $\theta_s$  (top) and Horizontal correlation length  $\zeta$  (bottom) for off-  
617 zenith angles up to  $20^\circ$  with respect to the zenith beam for East, West North, and South  
618 directions. Black dotted lines in the top and bottom panels correspond to the threshold  
619 values of  $3.093^\circ$  and 7.187 m for aspect angle and correlation length for the radar.

620 **Figure 9.** Effective beam pointing angle ( $\theta_{\text{eff}}$ ) for off-zenith angles.

621 **Figure 10.** Scatter plots of aspect sensitivity parameter ( $\text{SNR}_{\text{Zenith-Oblique}}$ ) against (a) wind  
622 shear (b) stability for East-West (top) and North-South (bottom) for July 22, 2022.

623 **Figure 11.** Height-time intensity plots of (a) SNR, (b) vertical velocity ( $w$ ) and (c)  
624 uncorrected half-power full spectral width for continuous zenith observations starting at  
625 14:10:23 LT on July 22, 2022.

626 **Figure 12.** Altitude profiles of (a) zonal and meridional winds derived from the radar, (b)  
627 temperature obtained from COSMIC-2 satellite for ( $9.63^\circ\text{N}$ ,  $76.12^\circ\text{E}$ ), (c) Stability, (d)  
628 wind Shear and (e) Richardson Number at 13:16:07 LT on July 22, 2022.

629 **Figure 13.** (a) Power spectra of vertical velocity at 14.8 and 15.7 km, height profiles of  
630 amplitude (left) and phase (right) for (b) 10-12 min, and (c) 16-18 min dominant periods  
631 during 14:10-17:30 LT on July 22, 2022.

632 **Figure 14.** Height profiles of (a) horizontal wind speed ( $U_h$ ), (b) vertical shear ( $S$ ) of  $U_h$ ,  
633 (c) observed spectral width ( $\sigma^2$ ) vertical beam (red) along with theoretical estimation for  
634 beam-broadening (black squares), and (d) observed spectral width in East (solid blue),  
635 West (dash blue), North (solid green), South (dash green) for 12 degree off-zenith along  
636 with DH model by considering both beam and shear broadening on July 22, 2022.

637 **Figure 15.** Altitude profiles of percentage of underestimating factor of horizontal wind  
638 ( $R$ ) on July 22, 2022.

639 **Table captions**

640 **Table 1.** Radar parameters of CUSAT ST Radar as used for the experiment.

641 **Table 2.** Beam configuration and sequence of scan azimuth and zenith scan angles for the  
642 four modes. Values in parentheses denote azimuth and zenith angle with (0,10) signifying  
643 North 10° tilt and the azimuthal angles follow the meteorological convention with  
644 (90,10),(180,0) and (270,0) as East 10°, South 10° and West 10° respectively.

**Figure 1.** Beam configurations for different modes of experiment. See Table 2 for details.

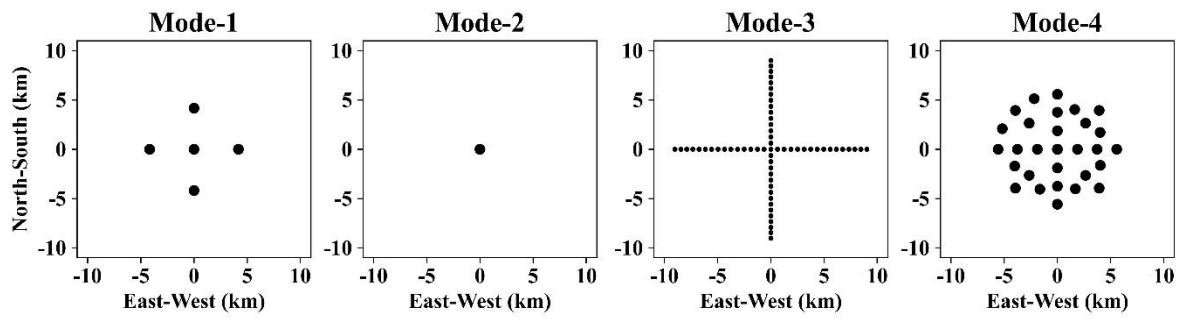


**Figure 2.** (a) Wind speed and direction (arrow) at 100 hPa, and (b) outgoing-long wave radiation along with mean sea level pressure at 13:30 LT on July 21 (left) and 22 (right), 2022. CUSAT ST radar is marked in each panels.

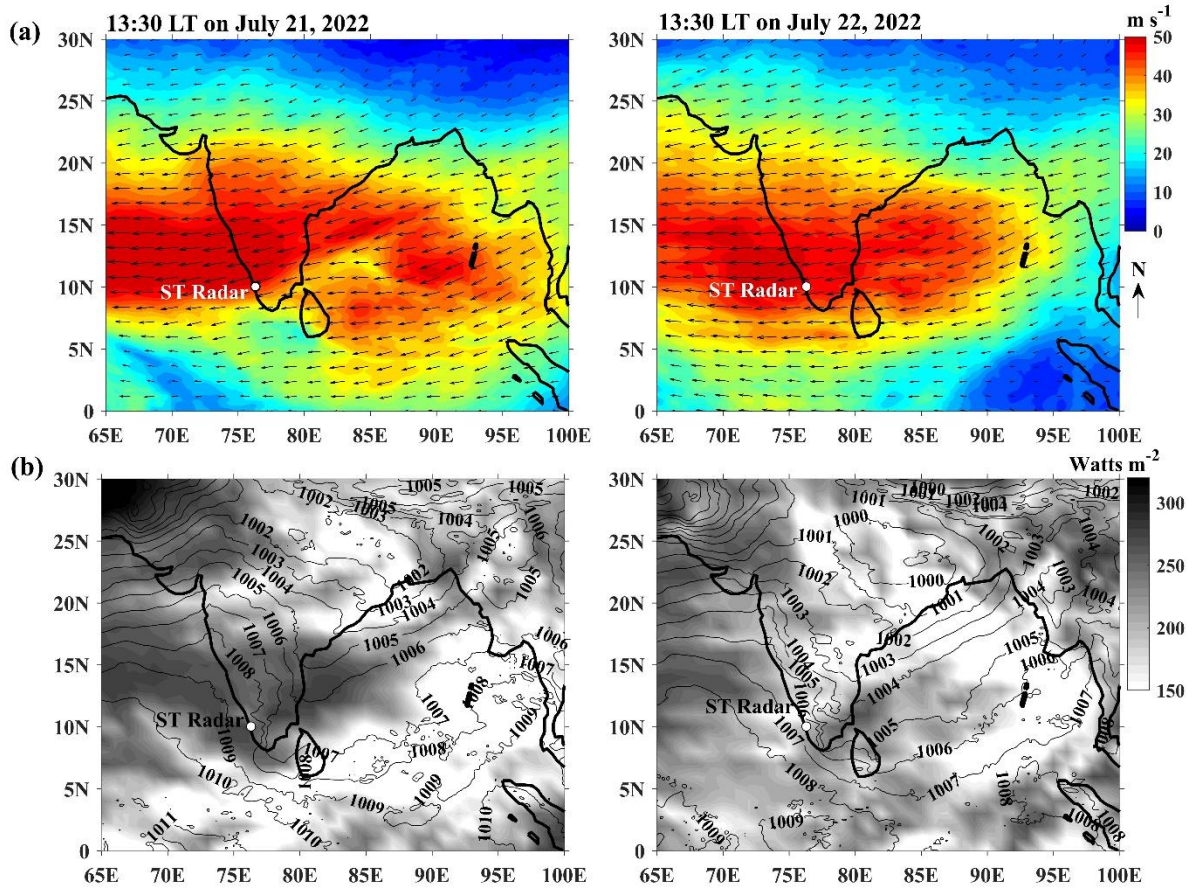


**Figure 3.** Fan sector maps in the E-W and N-S directions for (a) Signal-to-Noise (SNR), (b) Doppler velocity values, (c) uncorrected observed half-power full Spectral width at 13:30 LT on July 22, 2022.

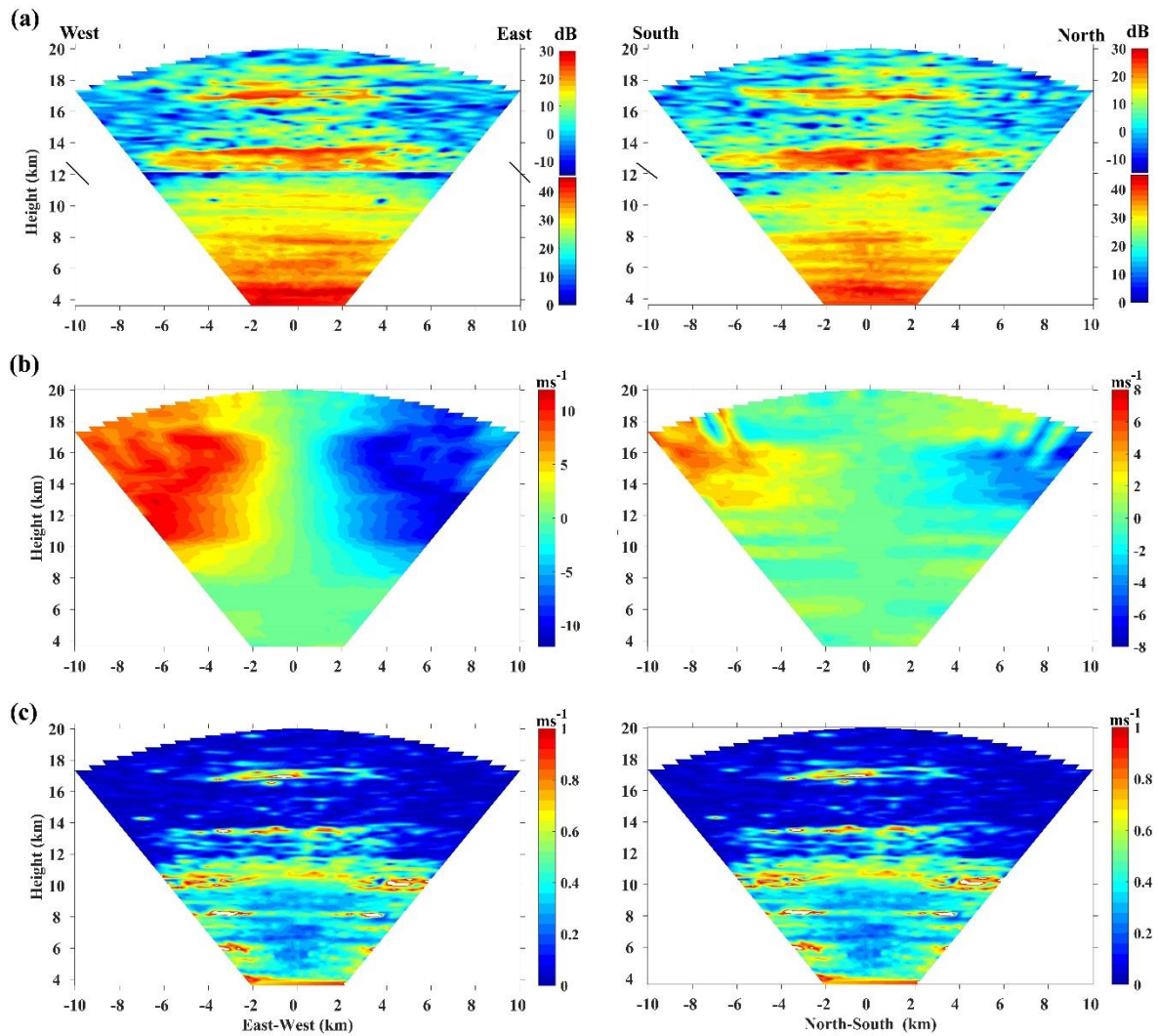


**Figure 4.** SNR as a function of zenith angles up to 30° in East-West (left) and North-South (right) directions for heights of 11.4 km, 12.4 km, 14 km and 16.4 km for July 22, 2022.

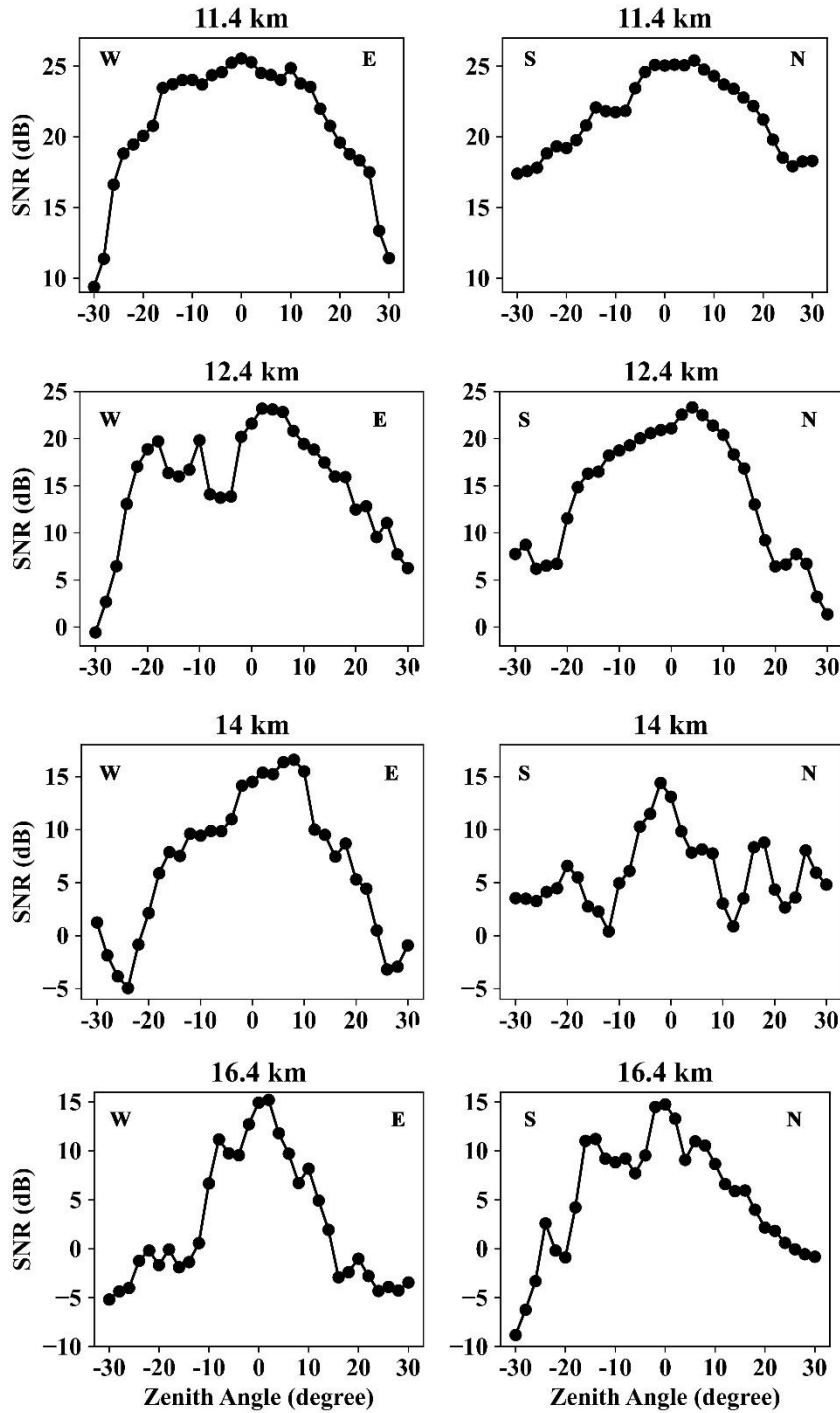


**Figure 5.** Doppler spectra as a function of zenith angle for July 22, 2022 for East-West (left) and North-South (right) planes.

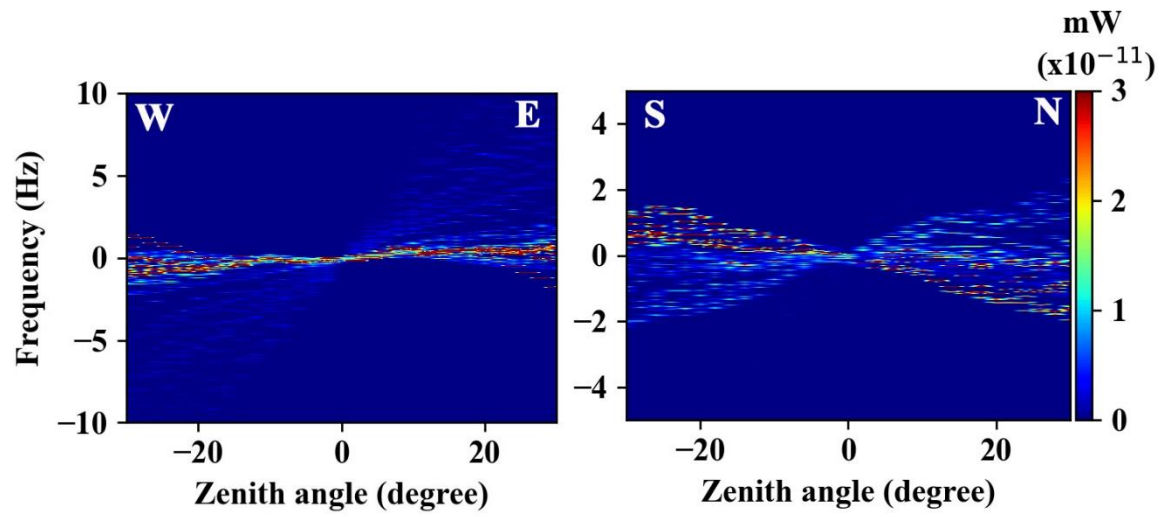


**Figure 6.** Volume scan slices at 14 km, 16 km and 17.6 km for (a) SNR, (b) Doppler, (c) uncorrected half-power full spectral width at 12 LT on July 22, 2022.

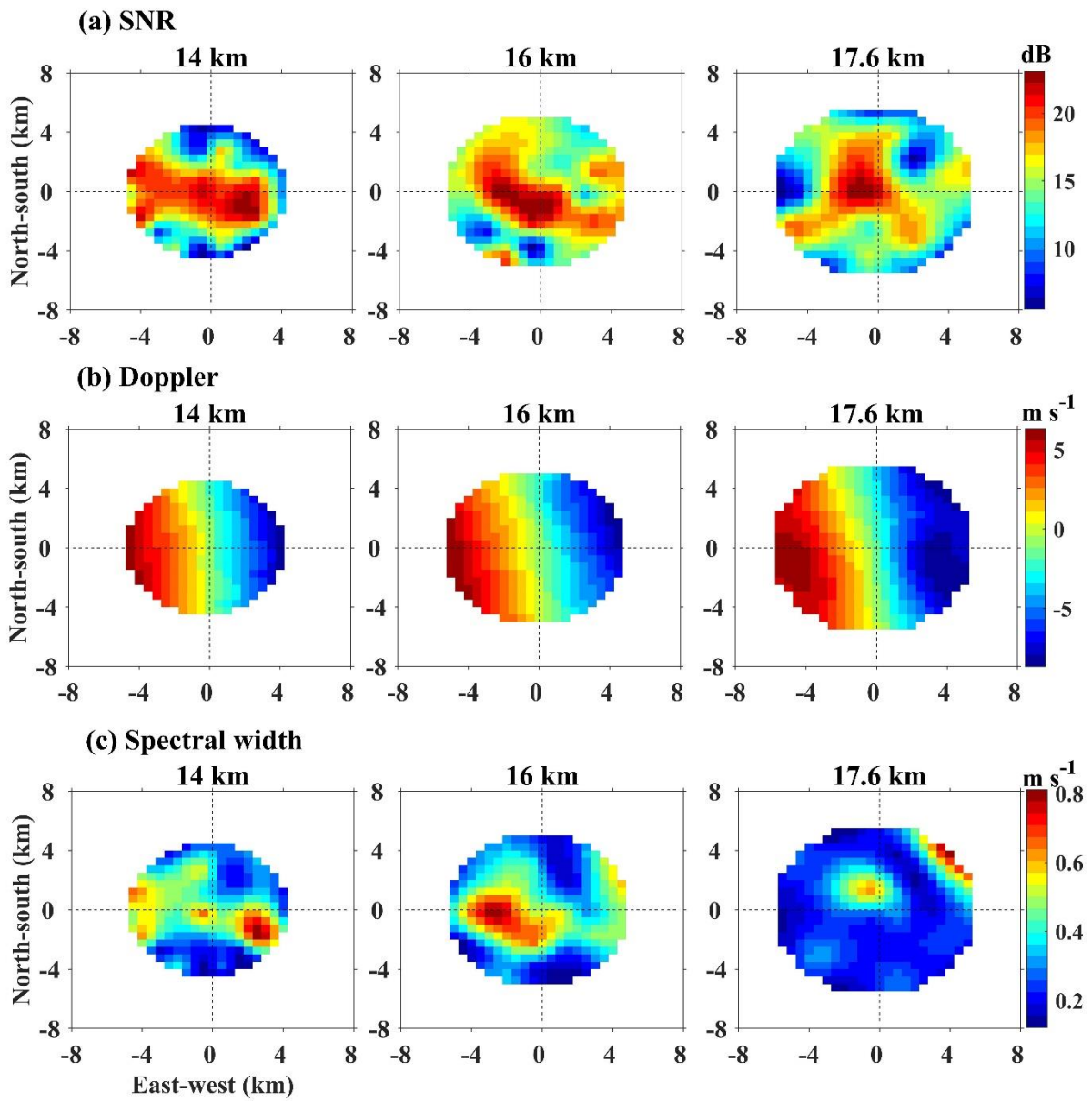


**Figure 7.** Altitude profiles of SNR difference between zenith and a few off-zenith angles for East, West, North, and South directions.

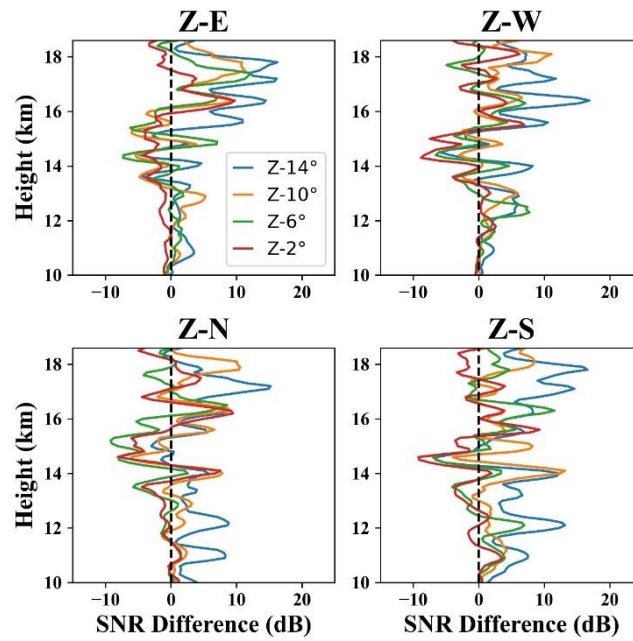


**Figure 8.** Aspect Angle  $\theta_s$  (top) and Horizontal correlation length  $\zeta$  (bottom) for off-zenith angles up to  $20^\circ$  with respect to the zenith beam for East, West North, and South directions. Black dotted lines in the top and bottom panels correspond to the threshold values of  $3.093^\circ$  and  $7.187$  m for aspect angle and correlation length for the radar.

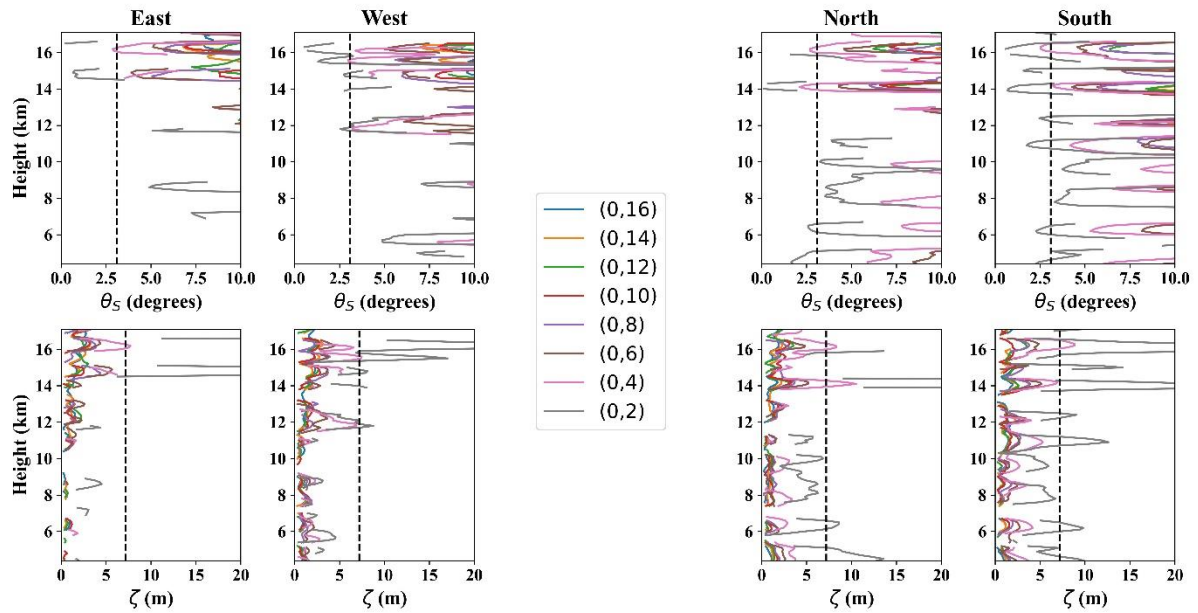


**Figure 9.** Effective beam pointing angle ( $\theta_{\text{eff}}$ ) for off-zenith angles.

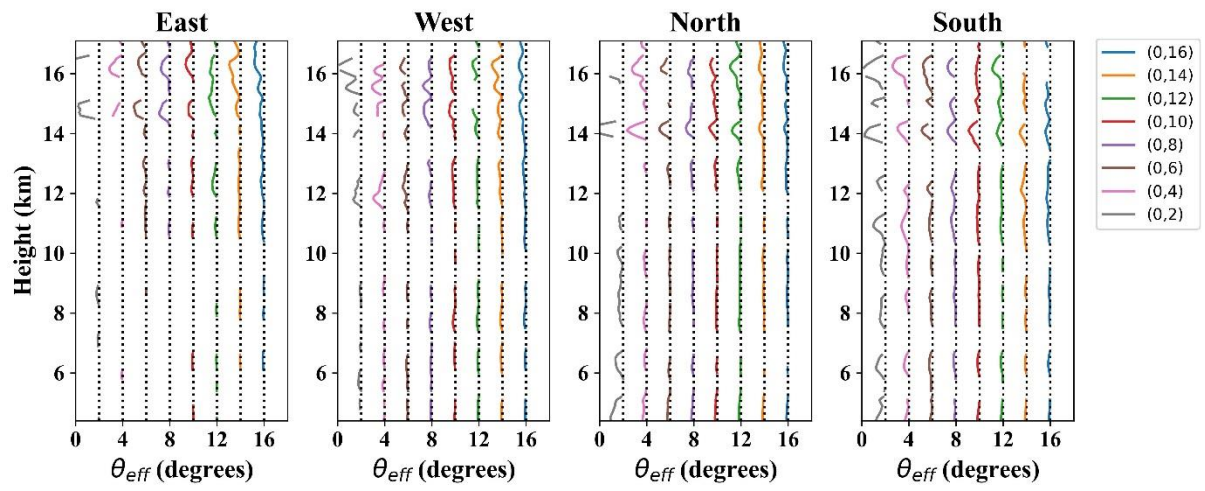


**Figure 10.** Scatter plots of aspect sensitivity parameter ( $\text{SNR}_{\text{Zenith-Oblique}}$ ) against (a) wind shear (b) stability for East-West (top) and North-South (bottom) for July 22, 2022.

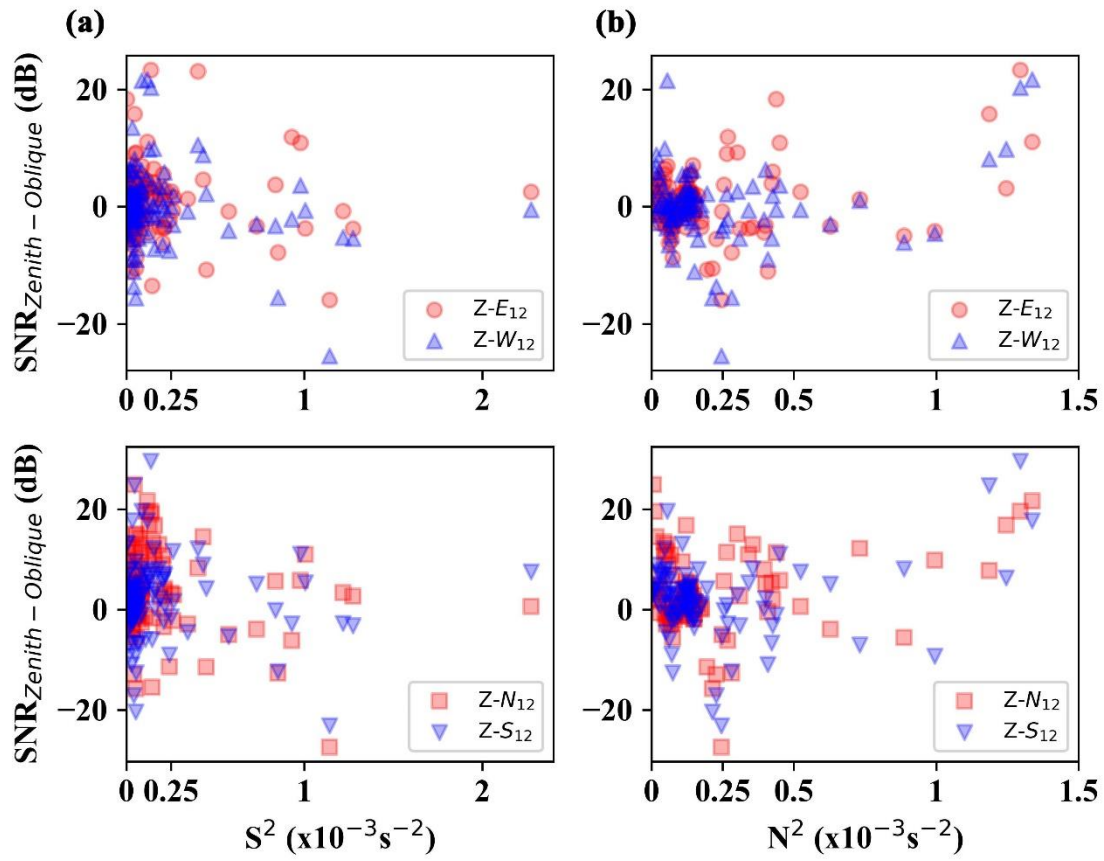


**Figure 11.** Height-time intensity plots of (a) SNR, (b) vertical velocity ( $w$ ) and (c) uncorrected half-power full spectral width for continuous zenith observations starting at 14:10:23 LT on July 22, 2022.

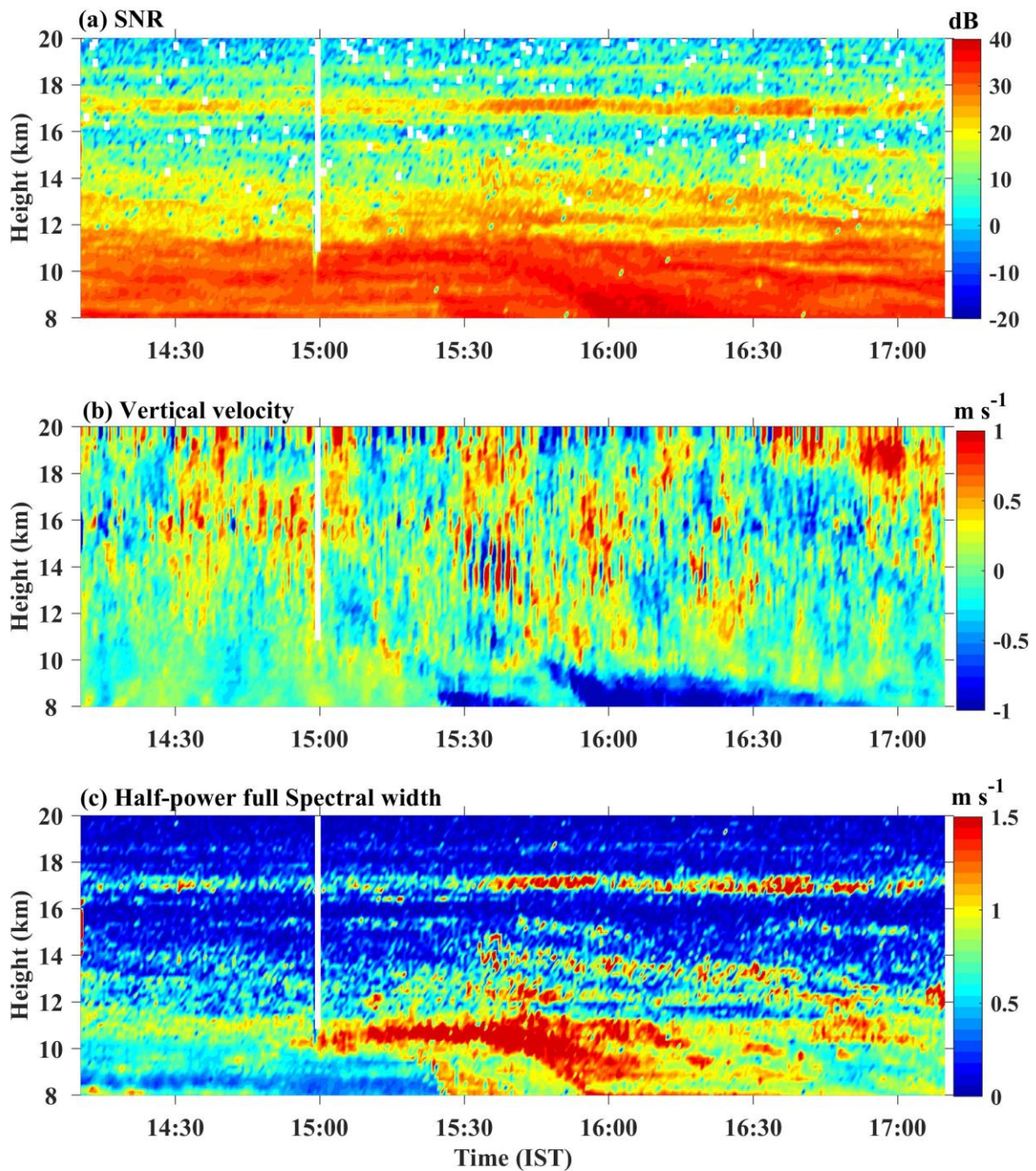


**Figure 12.** Altitude profiles of (a) zonal and meridional winds derived from the radar, (b) temperature obtained from COSMIC-2 satellite for (9.63°N, 76.12°E), (c) Stability, (d) wind Shear and (e) Richardson Number at 13:16:07 LT on July 22, 2022.

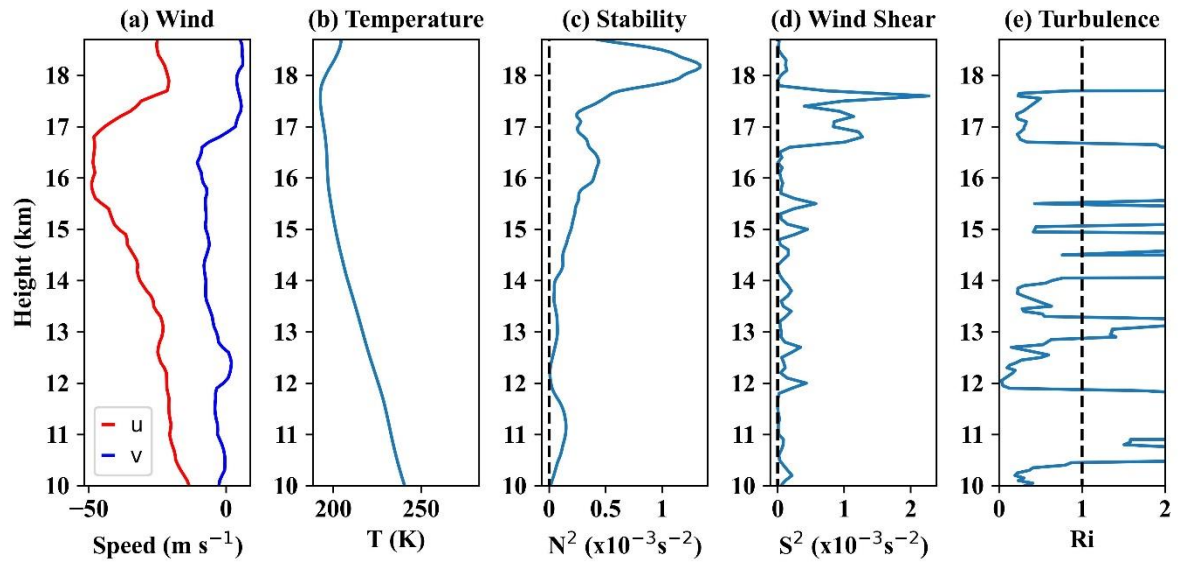


**Figure 13.** (a) Power spectra of vertical velocity at 14.8 and 15.7 km, height profiles of amplitude (left) and phase (right) for (b) 10-12 min, and (c) 16-18 min dominant periods during 14:10-17:30 LT on July 22, 2022.

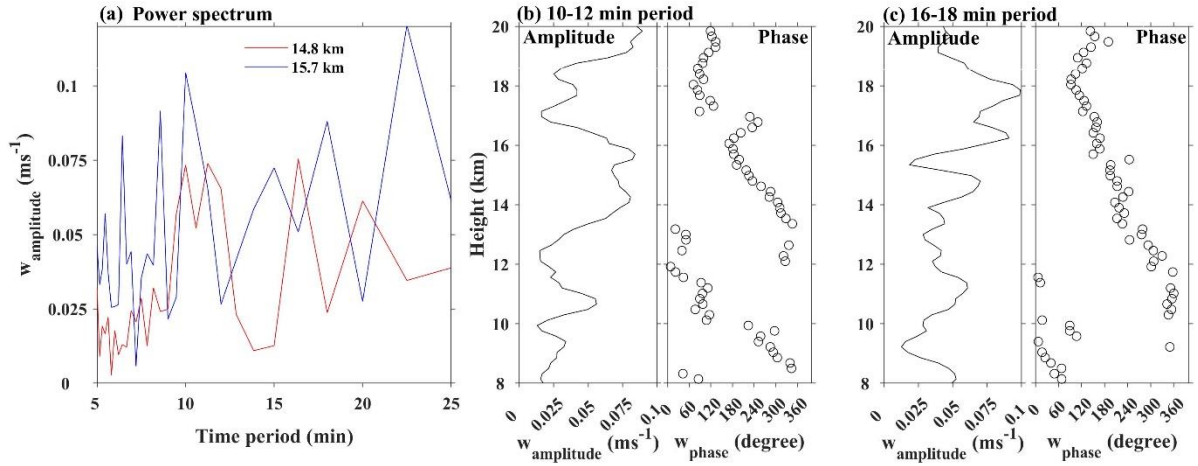


**Figure 14.** Height profiles of (a) horizontal wind speed ( $U_h$ ), (b) vertical shear ( $S$ ) of  $U_h$ , (c) observed spectral width ( $\sigma^2$ ) vertical beam (red) along with theoretical estimation for beam-broadening (black squares), and (d) observed spectral width in East (solid blue), West (dash blue), North (solid green), South (dash green) for 12 degree off-zenith along with DH model by considering both beam and shear broadening on July 22, 2022.

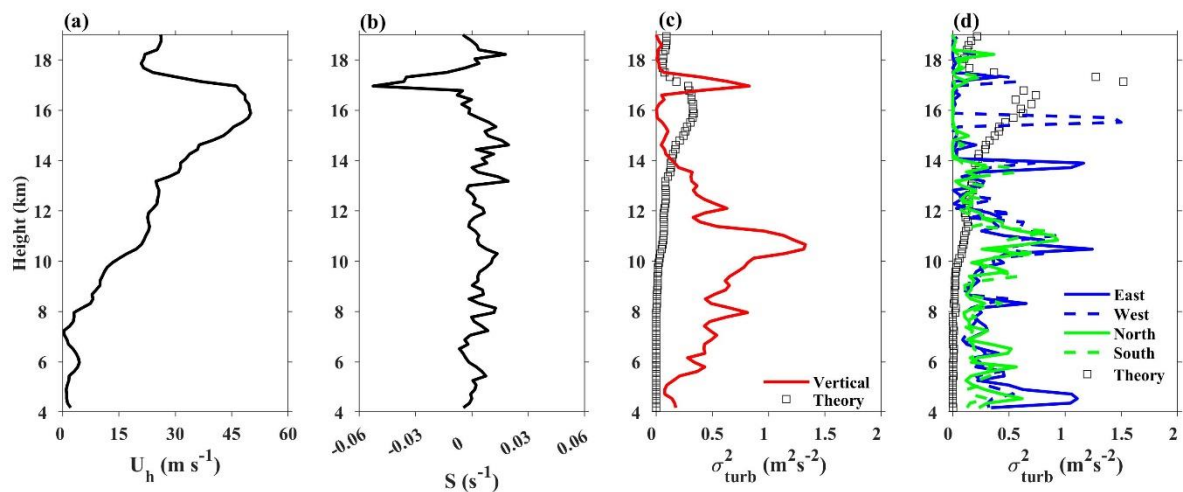


**Figure 15.** Altitude profiles of percentage of underestimating factor of horizontal wind (R) on July 22, 2022

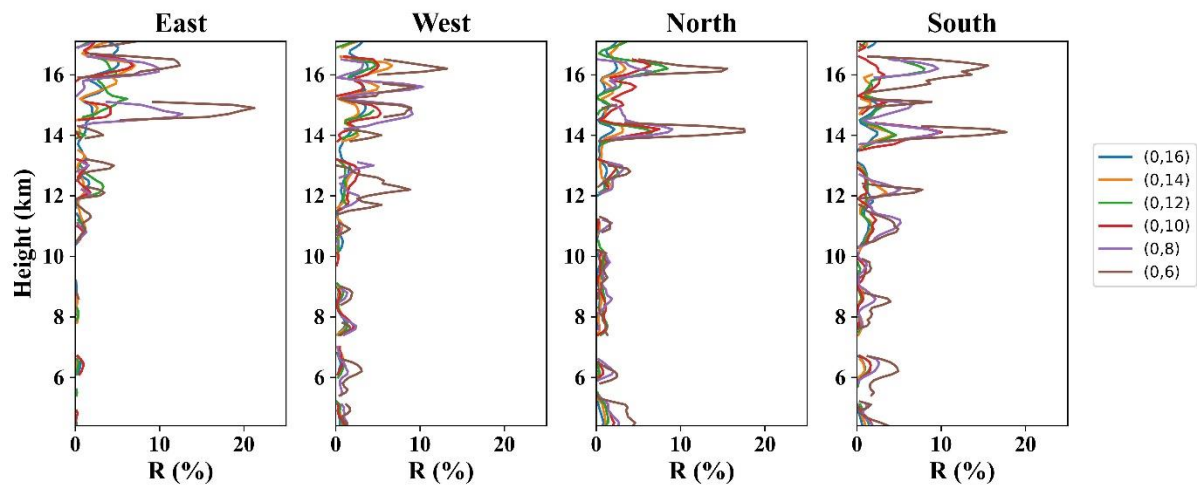


**Table 1.** Radar parameters of CUSAT ST Radar as used for the experiment.

<b>Parameter</b>	<b>Value</b>
Frequency	205MHz
Antenna	619 - 3 Element Yagi Uda Antenna
Mode of operation	Doppler Beam Swinging (DBS)
Peak Transmitted power	309 kW (TRM Peak power- 500 W)
Transmitted type	BPSK Modulation
Beam width	3°
Effective area	536 m <sup>2</sup>
Peak Power aperture product	~1.6 x10 <sup>8</sup> Wm <sup>2</sup>
Duty cycle	11.9%
Pulse width	19.2 μs
Inter Pulse Period (IPP)	161.29 μs
Pulse Code	Complementary/ Barker code
Range Resolution	180 m
No. of FFT points	1024
No. of Coherent Integrations	128
No. of Incoherent integrations	1
No. of Beams	31 / 61
Data format	ASCII

**Table 2.** Beam configuration and sequence of scan azimuth and zenith scan angles for the four modes. Values in parentheses denote azimuth and zenith angle with (0,10) signifying North 10° tilt and the azimuthal angles follow the meteorological convention with (90,10),(180,0) and (270,0) as East 10°, South 10° and West 10° respectively.

<b>Mode</b>	<b>Mode 1</b>	<b>Mode 2</b>	<b>Mode 3</b>	<b>Mode 4</b>
<b>Date</b>	21 and 22 July 2022	22 July 2022	21 and 22 July 2022	21 and 22 July 2022
<b>Time (LT)</b>	Day 1- 12:17:26-12:20:26 Day 2- 12:48:38-12:51:38	14:10:23-17:10:23	Day 1- 13:32:48-14:46:00 Day 2- 13:01:36-14:14:48	Day 1- 12:10:45-12:47:57 Day 2- 11:39:32-12:16:44
<b>No. of Scans</b>	2	6	2	2
<b>Azimuth and Zenith angles</b>	(90,12),(0,0), (270,12), (0,12),(180,12)	All (0,0)	(90,30),(90,28),..., (90,4),(90,2), (0,0),(270,2),(270,4) ,..., (270,28),(270,30), (0,30)(0,28),..., (0,4), (0,2),(180,2),(180,4) ,..., (180,28),(180,30)	(0,0),(0,6),(90,6),(180,6), (270,6),(0,0),(0,12),(45,12), (90,12),(135,12),(180,12), (225,12),(270,12),(315,12), (0,0),(0,18),(22,14),(45,18), (67,14),(90,18),(112,14), (135,18),(157,14),(180,18), (202,14),(225,18),(247,14), (270,18),(292,18),(315,18), (337,18)
<b>No. of beams</b>	5	50	61	31

## **Structures and backscattering characteristics of CUSAT 205 MHz Stratosphere-Troposphere Radar at Cochin (10.04°N, 76.3°E) - First results**

Nabarun Poddar<sup>1,2</sup>, Siddarth Shankar Das<sup>1,\*</sup>, Veenus Venugopal<sup>1,2</sup>, S. Abhilash<sup>3</sup>, V. Rakesh<sup>3</sup>

<sup>1</sup>Space Physics Laboratory, Vikram Sarabhai Space Centre, Thiruvananthapuram-695022

<sup>2</sup>Department of Physics, University of Kerala, Thiruvananthapuram

<sup>3</sup>Advanced Centre for Atmospheric Radar Research, Cochin University of Science and Technology, Cochin

e-mail: [dassiddhu@yahoo.com](mailto:dassiddhu@yahoo.com) & [siddarth\\_das@vssc.gov.in](mailto:siddarth_das@vssc.gov.in)

**Supplimentry material**

Figure S1. Same as Fig.3, but for July 21, 2022.

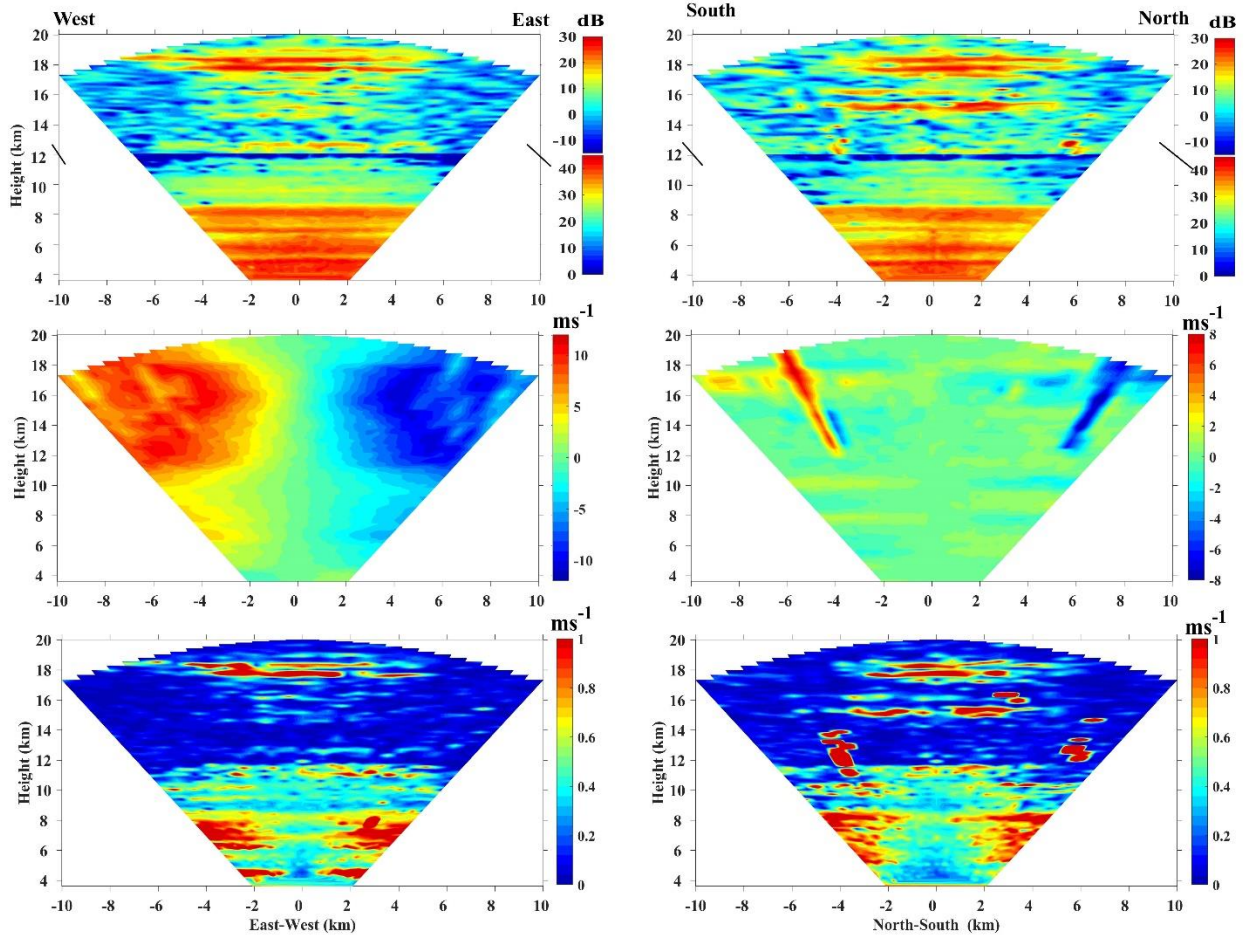
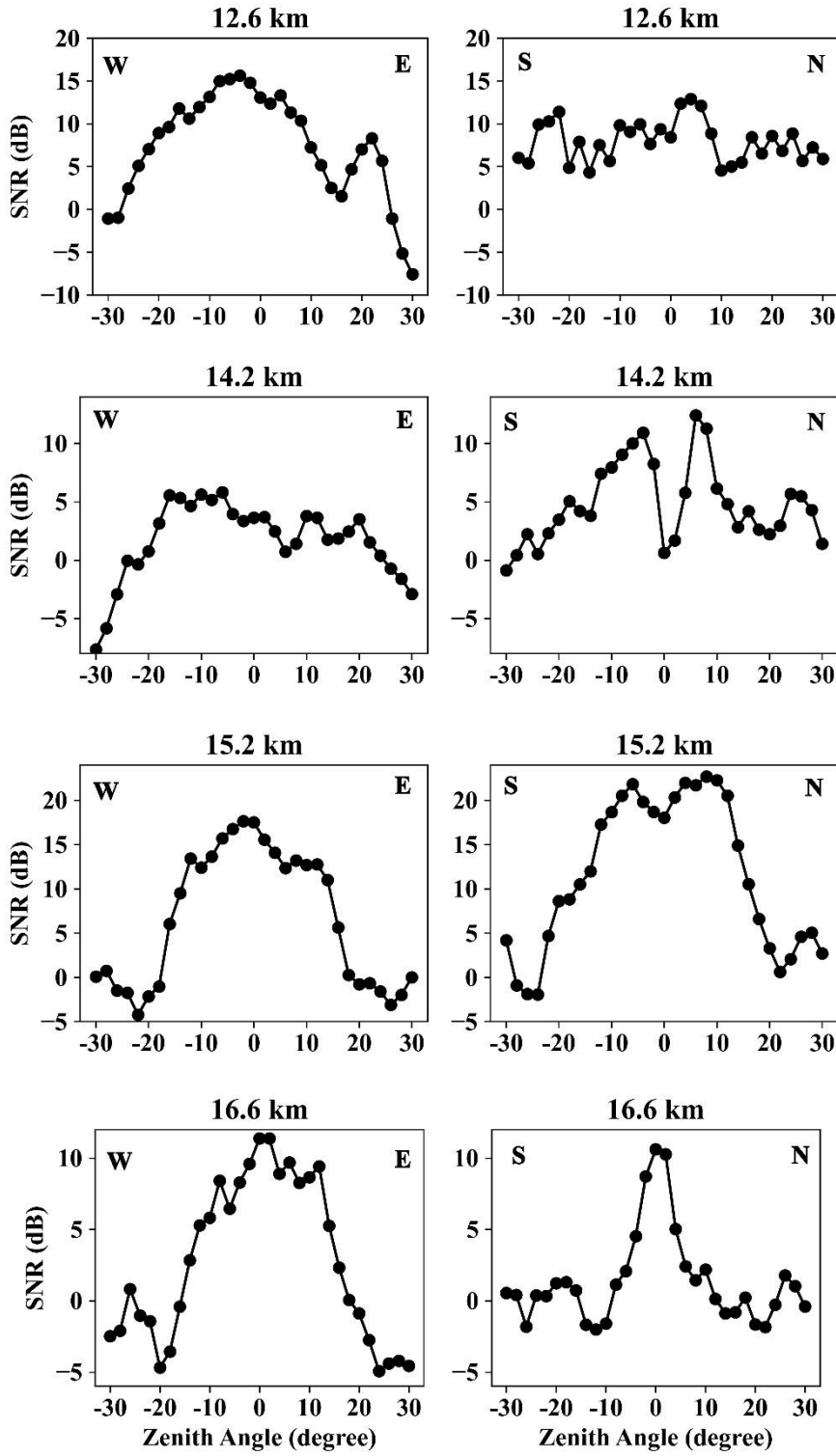
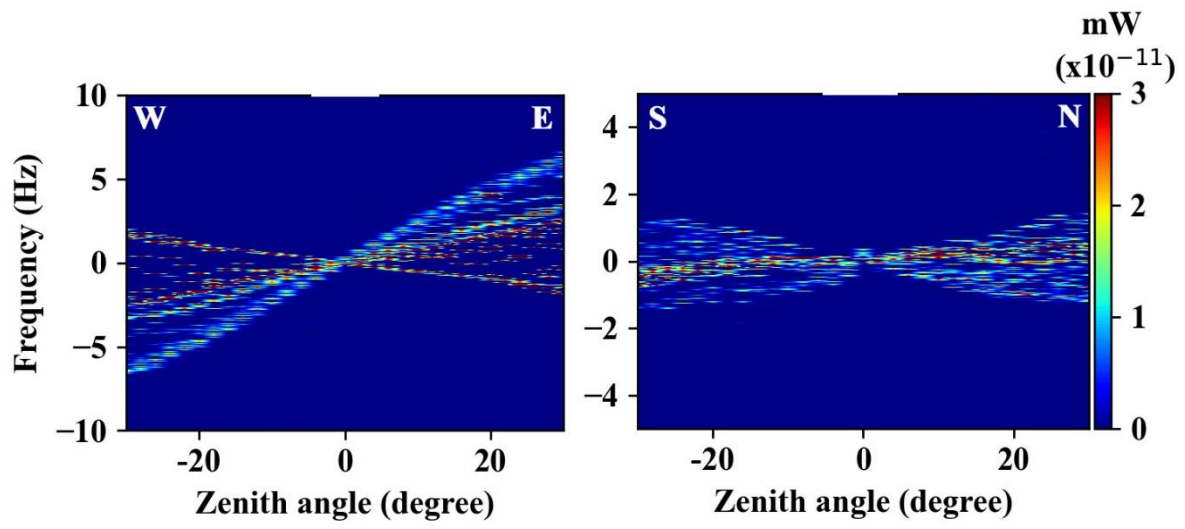


Figure S2. Same as Fig. 4, but for July 21, 2022.



**Figure S3.** Same as Fig. 5, but for July 21, 2022.



**Figure S4.** Same as Fig. 6, but for July 21, 2022.

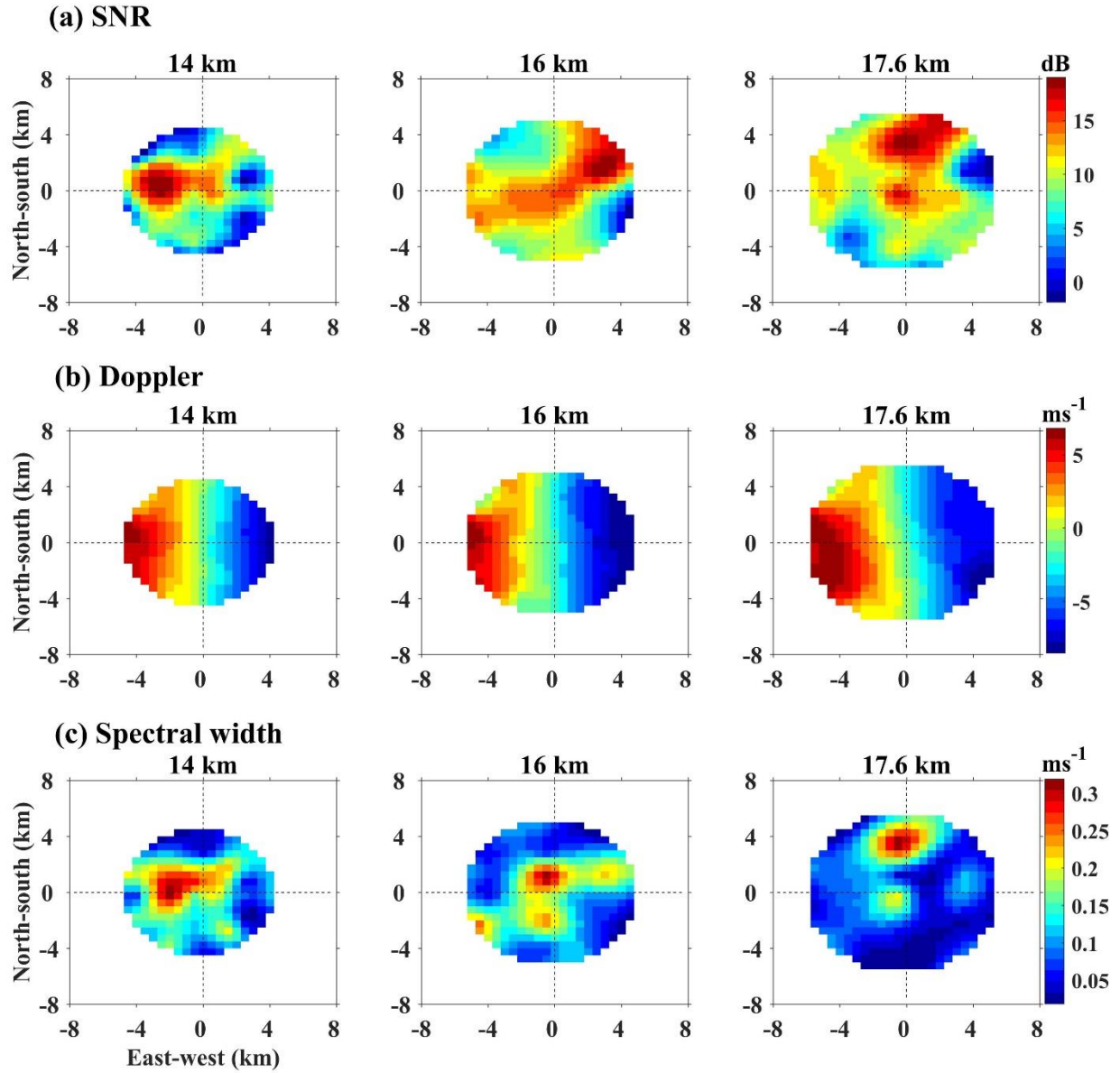


**Figure S5.** Same as Fig. 7, but for July 21, 2022.

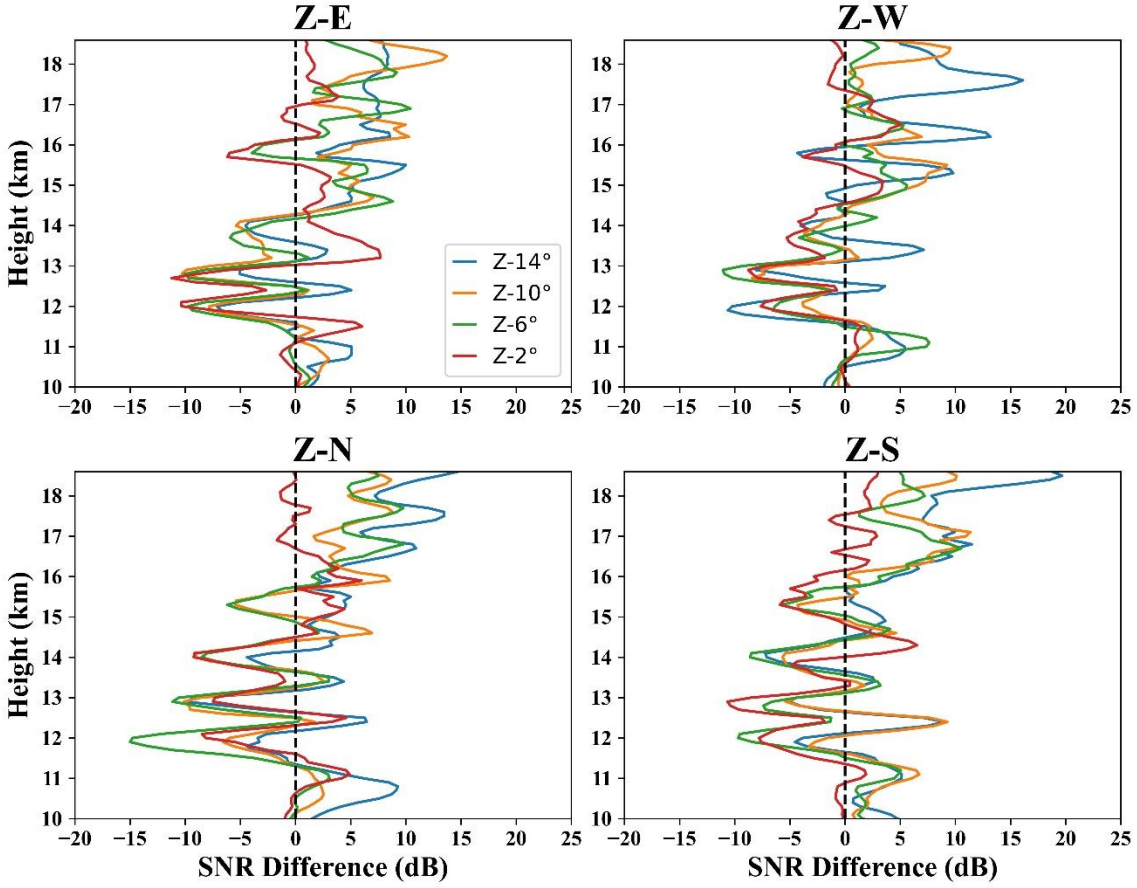


Figure S6. Same as Fig. 8, but for July 21, 2022.

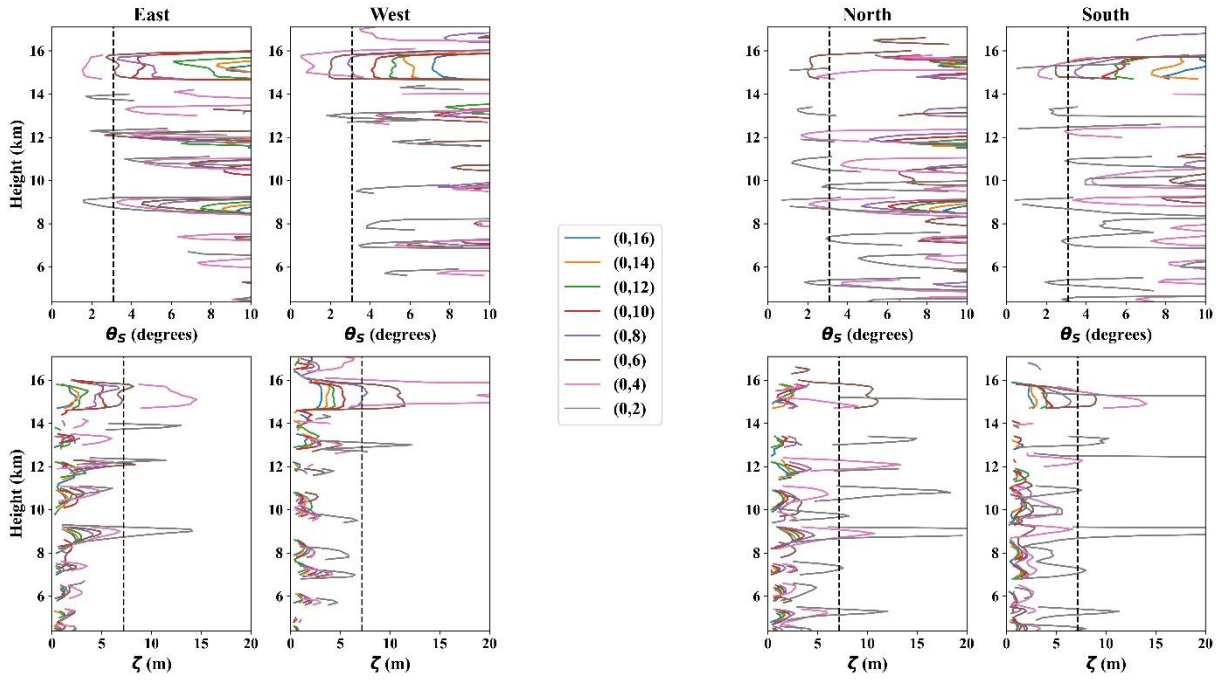


Figure S7. Same as Fig. 9, but for July 21, 2022.

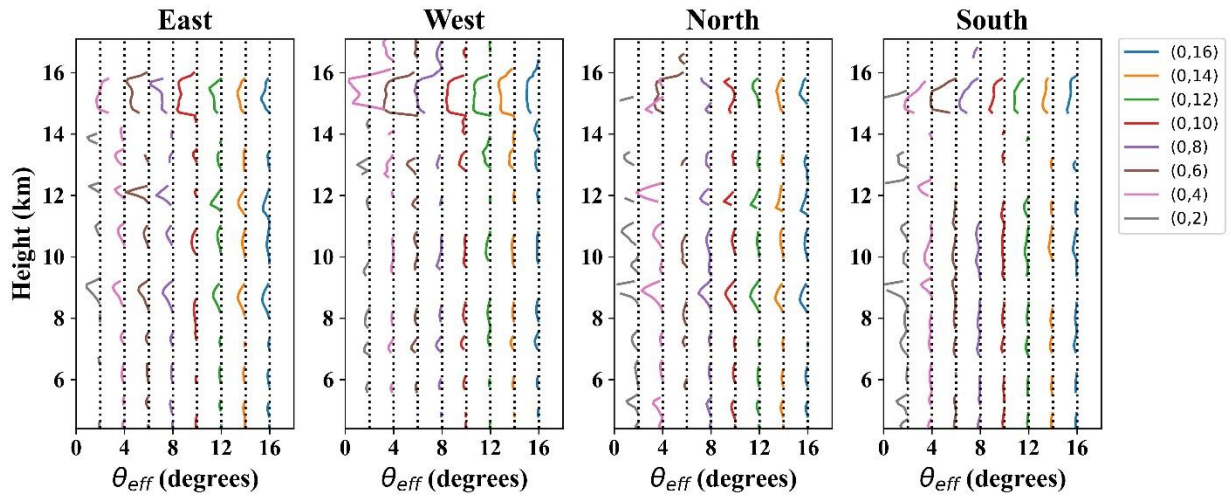


Figure S8. Same as Fig. 10, but for July 21, 2022.

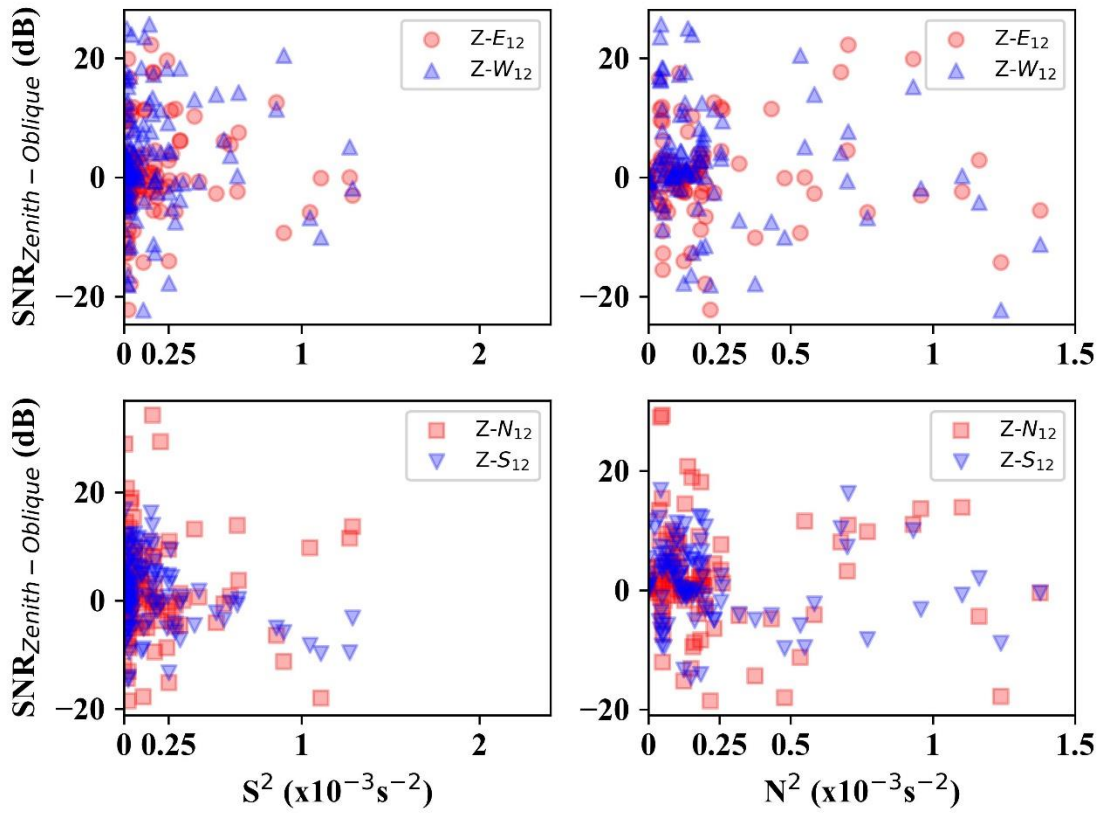
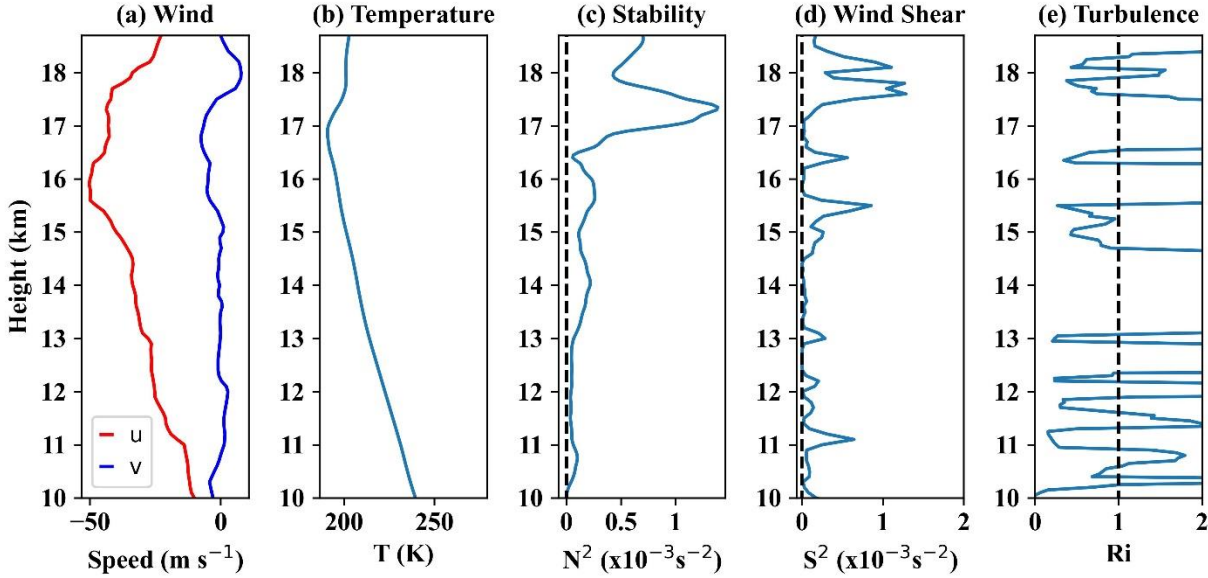


Figure S9. Same as Fig. 12, but for July 21, 2022.



**Figure S10.** Same as Fig. 15, but for July 21, 2022.

